8. Nielsen, H., Engelbrecht, J., Brunak, S. & von Heijne, G. Identification of prokaryotic and eukaryotic signal peptides and prediction of their cleavage sites. *Protein Eng.* **10,** 1–6 (1997).
9. Rouille, Y. *et al.* Proteolytic processing mechanisms in the biosynthesis of neuroendocrine peptides: the subtilisin-like proprotein convertases. *Front. Neuroendocrinol.* **16,** 322–361 (1995).
10. Nishimura, O. *et al.* Synthesis of new peptides with prolactin-releasing activity by a combination of recombinant DNA technology and a cysteine-specific cyanylation reaction. *Chem. Pharm. Bull. (Tokyo)* **46,** 1490–1492 (1998).
11. Turner, C. E. Paxillin and focal adhesion signalling. *Nature Cell Biol.* **2,** E231–E236 (2000).
12. Sadahira, Y., Ruan, F., Hakomori, S. & Igarashi, Y. Sphingosine 1-phosphate, a specific endogenous signaling molecule controlling cell motility and tumor cell invasiveness. *Proc. Natl Acad. Sci. USA* **89,** 9686–9690 (1992).
13. Yamamura, S., Hakomori, S., Wada, A. & Igarashi, Y. Sphingosine-1-phosphate inhibits haptotactic motility by overproduction of focal adhesion sites in B16 melanoma cells through EDG-induced activation of Rho. *Ann. NY Acad. Sci.* **905,** 301–307 (2000).
14. Bischof, P., Meisser, A. & Campana, A. Paracrine and autocrine regulators of trophoblast invasion. *Placenta* **21,** S55–S60 (2000).
15. Masuda, Y. *et al.* Receptor binding and antagonist properties of a novel endothelin receptor antagonist, TAK-044 [cyclo[D-alpha-aspartyl-3-[(4-phenylpiperazin-1-yl)carbonyl]-L-alanyl-L-aspartyl-D-2-(2-thienyl) glycyl-L-leucyl-D-tryptophyl]disodium salt], in human endothelin A and endothelin B receptors. *J. Pharmacol. Exp. Ther.* **279,** 675–685 (1996).
16. Fujii, R. *et al.* Identification of neuromedin U as the cognate ligand of the orphan G protein-coupled receptor FM-3. *J. Biol. Chem.* **275,** 21068–21074 (2000).
17. Linden, J. Calculating the dissociation constant of an unlabeled compound from the concentration required to displace radiolabel binding by 50%. *J. Cyclic Nucleotide Res.* **8,** 163–172 (1982).

Supplementary information is available on *Nature*'s World-Wide Web site (http://www.nature.com) or as paper copy from the London editorial office of *Nature*.

Acknowledgements

We thank R. Sasada, M. Mori, T. Henta, M. Harada, K. Oda and Y. Horikoshi for technical advice and assistance.

Correspondence and requests for materials should be addressed to T.O. (e-mail: Ohtaki_Tetsuya@takeda.co.jp). The nucleotide sequence data reported here will appear in the DDBJ/EMBL/GenBank nucleotide sequence databases with the accession numbers AB051065 (*hOT7175*) and AB051066 (*rOT7T175*).

erratum

Self-assembly of mesoscopically ordered chromatic polydiacetylene/silica nanocomposites

Yunfeng Lu, Yi Yang, Alan Sellinger, Mengcheng Lu, Jinman Huang, Hongyou Fan, Raid Haddad, Gabriel Lopez, Alan R. Burns, Darryl Y. Sasaki, John Shelnutt & C. Jeffrey Brinker

Nature **410,** 913–917 (2001)

A symbol was omitted from the author list. Yi Yang should have been denoted as contributing equally to this work with Yunfeng Lu. □

corrections

Formation cross-sections of singlet and triplet excitons in π-conjugated polymers

M. Wohlgenannt, Kunj Tandon, S. Mazumdar, S. Ramasesha & Z. V. Vardeny

Nature **409,** 494–497 (2001)

The molecular structure of the π-conjugated polymer mLPPP shown as an inset to Fig. 1a is incorrect; the correct structure is shown below. Furthermore, we regret not to have acknowledged U. Scherf and K. Muellen, who synthesized the mLPPP polymer. □

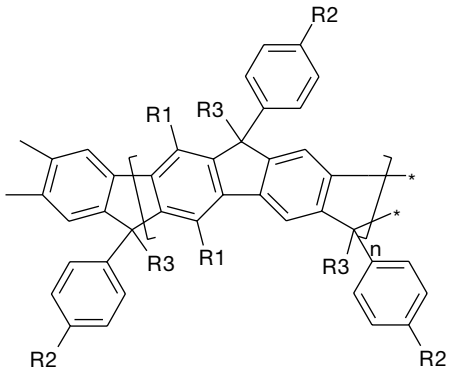

mLPPP (R1 = n-C_6H_{13}, R2 = n-$C_{10}H_{21}$ R3 = CH_3)

Crystal structure of the B7-1/CTLA-4 complex that inhibits human immune responses

Carin C. Stamper, Yan Zhang, James F. Tobin, David V. Erbe, Shinji Ikemizu, Simon J. Davis, Mark L. Stahl, Jasbir Seehra, William S. Somers & Lidia Mosyak

Nature **410,** 608–611 (2001)

The Protein Data Bank accession number given was incorrect. The correct accession number is 1I8L. □

8. Ramasastry, C. & Ramaiah, A. S. Electrical conduction in $Na_3H(SO_4)_2$ crystals. *J. Mater. Sci. Lett.* **16,** 2011–2016 (1981).
9. Chisholm, C. R. I., Merinov, B. V. & Haile, S. M. High temperature phase transitions in $K_3H(SO_4)_2$. *Solid State Ion.* (in the press).
10. Gaskell, D. R. *Introduction to Metallurgical Thermodynamics* 2nd edn, 574 & 586 (McGraw-Hill, Washington DC, 1981).
11. Srinivasan, S., Velev, O. A., Parthasarathy, A., Manko, D. J. & Appleby, A. J. High energy efficiency and high power density proton exchange membrane fuel cells—electrode kinetics and mass transport. *J. Power Sources* **36,** 299–320 (1991).
12. Croce, F. & Cigna, G. Determination of the protonic transference number for KH_2PO_4 by electromotive force measurements. *Solid State Ion.* **6,** 201–202 (1982).
13. Minh, N. Q. Ceramic fuel cells. *J. Am. Ceram. Soc.* **76,** 563–588 (1993).
14. Minh, N. Q. & Horne, C. R. in *Proc. 14th Risø Int. Symp. on Materials Science: High Temperature Electrochemical Behaviour of Fast Ion and Mixed Conductors* (eds Poulsen, F. W., Bentzen, J. J., Jacobsen, T., Skou, E. & Østergård, M. J. L.) 337–341 (Risø National Laboratory, Roskilde, 1993).
15. Baranov, A. I., Khiznichenko, V. P., Sandler, V. A. & Shuvalov, L. A. Frequency dielectric dispersion in the ferroelectric and superionic phases of CsH_2PO_4. *Ferroelectrics* **81,** 183–186 (1988).
16. Slade, R. C. T. & Omana, M. J. Protonic conductivity of 12-tungstophosphoric acid (TPA, $H_3PW_{12}O_{40}$) at elevated temperatures. *Solid State Ion.* **58,** 195–199 (1992).
17. Haile, S. M., Narayanan, S. R., Chisholm, C. & Boysen, D. Proton conducting membrane using a solid acid. US patent 09/439,377 (15 Nov. 2000).

Supplementary information is available on *Nature*'s World-Wide Web site (http://www.nature.com) or as paper copy from the London editorial office of *Nature*.

Acknowledgements

We thank J. Snyder for assistance with computer automation of the fuel cell test station and S. R. Narayanan for technical discussions. Financial support has been provided by the California Institute of Technology through the Yuen Grubstake entrepreneurial fund.

Correspondence and requests for materials should be addressed to S.M.H. (e-mail: smhaile@caltech.edu).

Self-assembly of mesoscopically ordered chromatic polydiacetylene/silica nanocomposites

Yunfeng Lu*†‡§, Yi Yang†, Alan Sellinger‡§, Mengcheng Lu†, Jinman Huang†, Hongyou Fan‡, Raid Haddad†, Gabriel Lopez†, Alan R. Burns‡, Darryl Y. Sasaki‡, John Shelnutt‡ & C. Jeffrey Brinker†‡

† *The University of New Mexico Center for Micro-Engineered Materials and Department of Chemical and Nuclear Engineering, Albuquerque, New Mexico 87131, USA*
‡ *Sandia National Laboratories, Advanced Materials Laboratory, 1001 University Blvd SE, Albuquerque, New Mexico 87106, USA*
* *These authors contributed equally to this work.*

Nature abounds with intricate composite architectures composed of hard and soft materials synergistically intertwined to provide both useful functionality and mechanical integrity. Recent synthetic efforts to mimic such natural designs have focused on nanocomposites[1–5], prepared mainly by slow procedures like monomer or polymer infiltration of inorganic nanostructures[6,7] or sequential deposition[8,9]. Here we report the self-assembly of conjugated polymer/silica nanocomposite films with hexagonal, cubic or lamellar mesoscopic order using polymerizable amphiphilic diacetylene molecules as both structure-directing agents and monomers. The self-assembly procedure is rapid and incorporates the organic monomers uniformly within a highly ordered, inorganic environment. Polymerization results in polydiacetylene/silica nanocomposites that are optically transparent and mechanically robust. Compared to ordered diacetylene-containing films prepared as Langmuir monolayers[10] or by Langmuir–Blodgett deposition[10], the nanostructured inorganic host alters the diacetylene polymerization behaviour, and the resulting nanocomposite exhibits unusual chromatic changes in response to thermal, mechanical and chemical stimuli. The inorganic framework serves to protect, stabilize, and orient the polymer, and to mediate its function. The nanocomposite architecture also provides sufficient mechanical integrity to enable integration into devices and microsystems.

Owing to extended π-electron delocalization along their backbones, conjugated organic polymers exhibit electronic and optical properties of interest for applications ranging from light-emitting diodes to biomolecular sensors[11]. For example, in blue-coloured polydiacetylene, the optical absorption blue-shifts dramatically when stress is applied to the backbone through the pendant side chains, and this thermally, mechanically, or chemically induced chromatic (blue → red) response has been explored as a colorimetric transduction scheme in a variety of chemically and physically based sensor designs[12,13]. Further improvements of the electronic and optical performance of conjugated polymer devices may require polymer incorporation in nano-engineered architectures[14] that could provide alignment, control charge and energy transfer, mediate conformational changes and prevent oxidation. Recently control of energy transfer was demonstrated in a poly[2-methoxy-5-(2′-ethyl-hexyloxy-)-1,4-phenylene vinylene] (MEH-PPV)/silica nanocomposite[7]. However, this nanocomposite, prepared by MEH-PPV infiltration of a pre-formed, oriented, hexagonal, silica mesophase, was heterogeneous, exhibiting two distinct conjugated polymer environments, that is, polymers inside and outside the hexagonally arranged pore channels of the silica particles. In general, because polymer infiltration into a pre-formed porous nanostructure depends on the partitioning of the polymer from the solvent, we expect it to be difficult to control polymer concentration, orientation and uniformity in the corresponding nanocomposite. Further, when the nanostructure pore size is less than the radius of gyration of the solvated polymer, infiltration proceeds by a worm-like motion referred to as reptation, requiring long processing times at elevated temperatures[7].

We use a series of oligoethylene glycol functionalized diacetylenic (DA-EO_n) surfactants (structure **1**, with $n = 3$, 4 5, or 10), prepared by coupling ethylene glycols with the acid chloride of PCA (structure **2**)

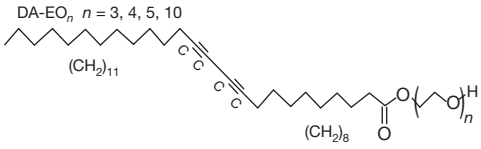

1

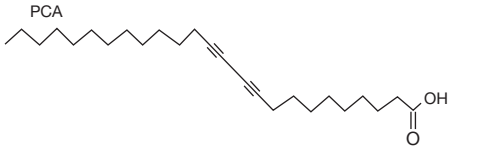

2

both as amphiphiles to direct the self-assembly of thin film silica mesophases[15] and as monomeric precursors of the conjugated polymer, polydiacetylene (PDA). Beginning with a homogeneous solution of silicic acid and surfactant prepared in a tetrahydrofuran (THF)/water solvent with initial surfactant concentration c_o much less than the critical surfactant micelle concentration CMC, we use evaporative dip-coating, spin-coating, or casting procedures to prepare thin films on silicon ⟨100⟩ or fused silica substrates (Fig. 1). During deposition, preferential evaporation of THF

§ Present address: Tulane University Chemical Engineering Department, New Orleans, Louisiana 70118, USA (Y.L.); Canon Research and Development Center Americas, San Jose, California 95134, USA (A.S.).

concentrates the depositing film in water and nonvolatile silica and surfactant species. The progressively increasing surfactant concentration drives self-assembly of diacetylene/silica surfactant micelles and their further organization into ordered, three-dimensional, liquid crystalline mesophases. Ultraviolet-light-initiated polymerization of the DA units, accompanied by catalyst-promoted siloxane condensation, topochemically converts the colourless mesophase into the blue PDA/silica nanocomposite, preserving the highly ordered, self-assembled architecture.

The choice of surfactant greatly influences the resultant mesostructure. This is evident from the X-ray diffraction (XRD) patterns and TEM micrographs shown in Figs 2 and 3 for nanocomposites prepared from diacetylenic surfactants with tri ($n = 3$), penta ($n = 5$) and decaethylene ($n = 10$) glycol head groups. Increasing values of n increase the surfactant head group area a_o. This in turn reduces the value of the surfactant packing parameter, $g = v/a_o l$, where v is the surfactant volume and l the tail length[16], favouring the formation of progressively higher-curvature mesophases: lamellar ($n = 3$) → hexagonal ($n = 5$) → cubic ($n = 10$). From the highly ordered nanocomposite mesostructures observed by transmission electron microscopy (TEM), we infer that the surfactant monomers/structure-directing agents are uniformly organized into precise spatial arrangements before polymerization. These arrangements establish the proximity (topochemistry) of the reactive diacetylenic moieties and thus strongly influence the PDA polymerization process. This is best illustrated by comparing their polymerization behaviour, as shown by the blue (or red) colour of nanocomposite films prepared with different mesostructures (that is, the hexagonal, cubic, and lamellar mesostructures shown in Fig. 3) and contrasting these behaviours with those of planar self-assembled monolayer and trilayer films formed by Langmuir–Blodgett deposition of the neat DA surfactants.

Figure 4 shows a patterned blue PDA/silica nanocomposite film, with a hexagonal mesostructure (prepared using structure **1**, with $n = 5$), formed by ultraviolet exposure through a mask; the corresponding patterned red film was formed subsequently by heating to 100 °C (Fig. 4b). Whereas lamellar mesophases (prepared using structure **1** with $n = 3$) show qualitatively similar behaviour, cubic mesostructures (prepared using structure **1** with $n = 10$) and Langmuir monolayers and trilayers (prepared using neat **1** with $n = 3$, 5 or 10) remain colourless upon ultraviolet exposure and during heating. The different behaviour of lamellar and Langmuir films emphasize the importance of the nanostructured inorganic host on PDA polymerization. In both systems the diacetylenic

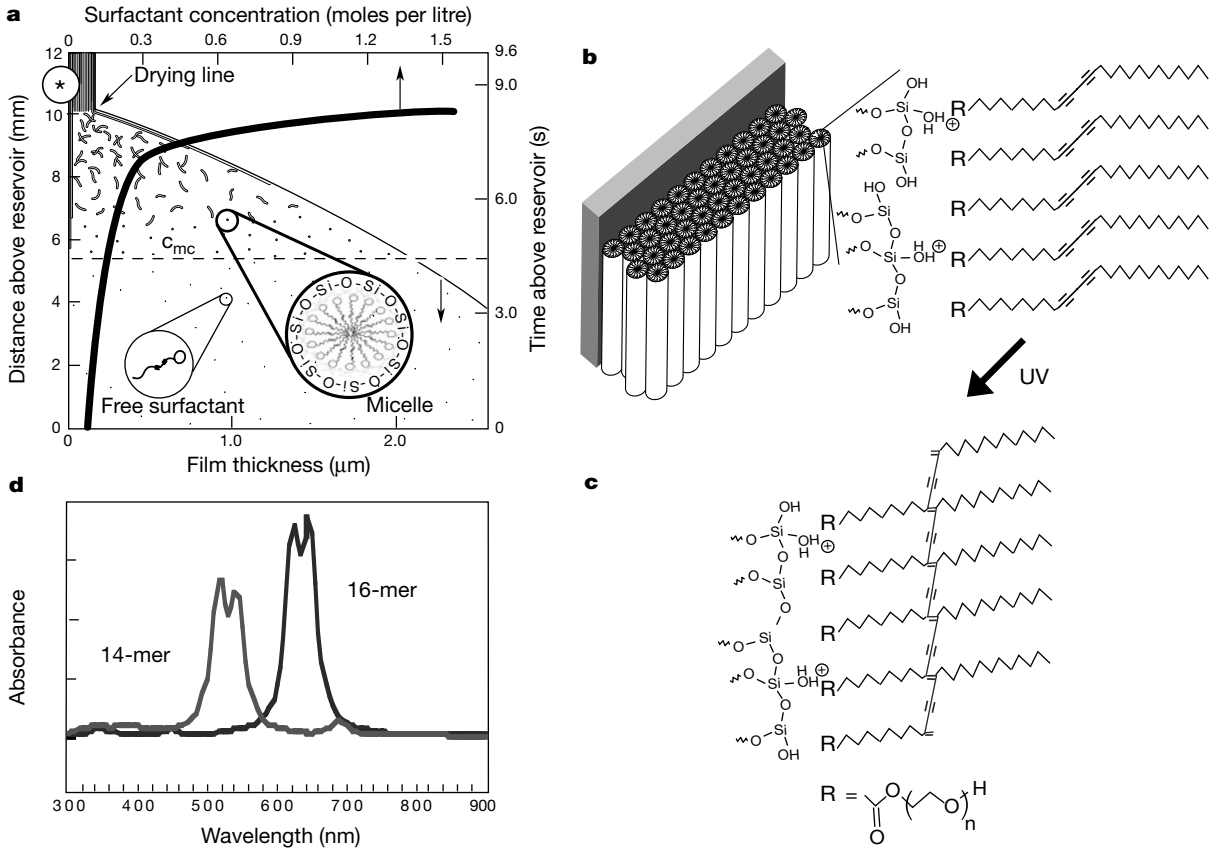

Figure 1 Schematic representation of the PDA/silica nanocomposite evaporation-induced self-assembly process. **a**, Steady-state film thickness and surfactant concentration profiles developed during dip-coating, with vertical axes representing distance and time above reservoir surface and horizontal axes showing film thickness and surfactant (structures **1** or **2**) concentration for $c_o = 0.034$ M. Beginning with a homogeneous solution prepared with $c_o <$ CMC, preferential THF evaporation induces micellization and further self-organization of silica–surfactant composite micelles into ordered thin-film mesophases. The shape and concentration of the DA surfactants influence the mesophase established at the drying line (lamellar, hexagonal or cubic). **b**, Section near asterisk shows a hexagonal mesostructure and hypothetical arrangement of DA surfactants adjacent to the cylindrically structured silicic acid framework. **c**, Hypothetical structure of polymerized PDA/silica nanocomposite formed upon exposure to ultraviolet light and continued acid-catalysed siloxane condensation. **d**, Ultraviolet–visible spectra of cyclic polydiacetylene oligomers determined by INDO/S (Intermediate Neglect Differential Orbital Spectra) quantum calculations after energy-optimization and 10 ps of molecular dynamics. The 16-membered oligomer with diameter of about 2.4 nm absorbs in the red region of the visual spectrum with spectral characteristics commensurate with the blue form of PDA (compare with Fig. 4e). The higher-curvature 14-membered PDA oligomer is strained and has a blue-shifted absorption spectrum consistent with the red form of PDA (compare with Fig. 4e).

surfactants are organized into highly oriented planar configurations with the EO headgroups disposed toward the hydrophilic interface, either water (Langmuir films) or polysilicic acid (nanocomposites). Despite these similar organizations, we suggest that Langmuir films do not polymerize because the reactive DA moieties are spaced too far apart, as indicated by the molecular areas measured at $30\,mN\,m^{-1}$ in a Langmuir trough: DA-EO_1 = 24 Å^2, DA-EO_3 = 38 Å^2, DA-EO_5 = 46 Å^2. Closer spacing of the EO headgroups (and correspondingly the diacetylenic moieties) within the self-assembled nanocomposites (lamellar, hexagonal or cubic) is anticipated from the requirement for charge density matching at the R-$EO_{n-y}[EO{\cdot}H_3O^+]_y{\cdot\cdot}yX^-{\cdot\cdot}wI^{\delta+}$ interface (where R = alkyl chain, $y \leq n$, $X = Cl^-$, $I^{\delta+}$ = the silica framework carrying a partial charge of δ^+, and w is the 'concentration' of framework needed for charge balance) that reduces the optimal EO headgroup area a_o (ref. 17). This closer spacing is reflected in measurements of the biaxial stress resulting from PDA polymerization, where, for nanocomposites, we observe development of compressive stress upon polymerization (film turns blue) and during the solvatochromic or thermochromic blue → red transformation; this indicates a net expansion of the PDA relative to the silica host (see Fig. A in the Supplementary Information). The corresponding neat DA surfactants prepared as Langmuir monolayers do not polymerize and develop no stress upon ultraviolet irradiation. Polymerizable DA Langmuir monolayers and multilayers (prepared using surfactants with smaller headgroups) contract upon polymerization and the magnitude of this contraction is used to assess the extent of polymerization[18].

The importance of the proximity of the DA moieties on polymerization is further illustrated by our inability to polymerize DA within the cubic mesophase prepared with $n = 10$ (see Fig. 3b and c). The large EO_{10} surfactant headgroups are necessary to direct the formation of the cubic mesophase, but they also serve as spacers preventing polymerization. Introduction of structure **1**, with $n = 3$ or 5 or structure **2** as co-surfactants with smaller headgroups (30–50 wt% relative to EO-DA_{10}) allows us to form cubic mesophases and to polymerize the mixed surfactant assemblies into the blue and red forms of PDA. (We expect that, owing to phase separation[19], this is not possible in Langmuir monolayers or Langmuir–Blodgett films).

The polymerization of the surfactant is highly dependent upon the topological alignment of diacetylenic units within the supramolecular assembly[20,21]. Additionally, for colorimetric materials to form (especially blue-coloured materials), the degree of polymerization and conjugation length of the 'ene'–'yne' backbone must be considerable[22]. The micellar structures that template the silica sol–gel material must thus contain highly oriented, densely packed surfactants. This packing will allow facile topochemical polymerization of the diacetylene units to give coloured polydiacetylene.

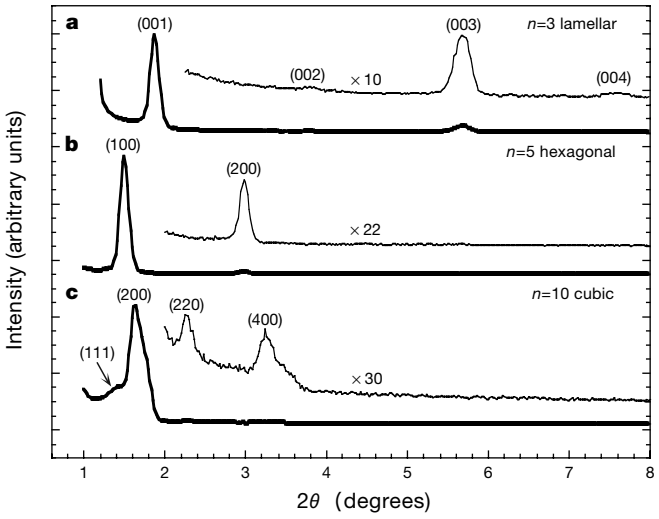

Figure 2 X-ray diffraction (XRD) patterns of nanocomposite thin films prepared using DA-EO_n (where $n = 3$, 5, and 10) surfactants. Increasing values of n increase the surfactant head group favouring the formation of progressively higher-curvature mesophases: lamellar ($n = 3$) → hexagonal ($n = 5$) → cubic ($n = 10$). **a**, Film prepared using 1.86% of DA-EO_3 (wt% DA-EO_3 relative to the solution weight without surfactant) shows a lamellar mesostructure with (001) diffraction peak at 48 Å. The presence of higher-order diffraction peaks (002), (003) and (004) indicate the formation of highly ordered alternating silica/PDA layers. **b**, Film prepared with DA-EO_5 (2.23%) shows a hexagonal mesophase with strong (100) and (200) diffraction peaks at 56 Å and 28 Å, respectively. **c**, Film prepared using 2.23% DA-EO_{10} surfactant exhibits a cubic mesophase with unit-cell parameter a = 108.1 Å. The presence of the (111) diffraction peak at 62.4 Å and the (200) diffraction peak at 54.1 Å clearly establishes a face-centred or primary cubic structure. The presence of higher-order peaks (220) at 38.2 Å and (400) at 27.3 Å provide further evidence of the primary or face-centred cubic mesophase. Introduction of structure **1**, with $n = 3$ or 5 or structure **2**, as co-surfactants with smaller headgroups (30–50 wt% relative to EO-DA_{10}) was necessary to polymerize PDA in the blue or red forms within the cubic mesophase. The XRD patterns were essentially unchanged by these co-surfactant additions.

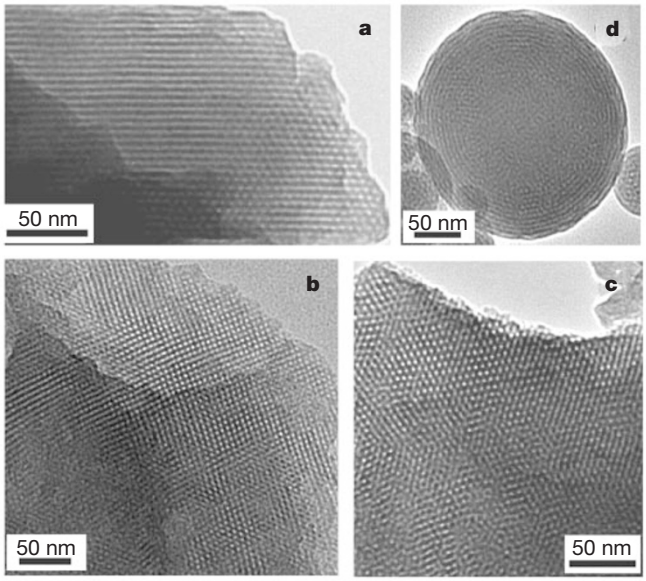

Figure 3 Representative transmission electron microscope (TEM) images of nanocomposite thin films (prepared as in Fig. 2b and c) and particles (formed by a related aerosol-assisted evaporation-induced self-assembly approach[32]). **a**, Hexagonally ordered nanocomposite prepared using 2.23% DA-EO_5 surfactant, showing a striped [110]-oriented mesophase with repeat distance around 48 Å and a region of the corresponding hexagonally patterned mesostructure characteristic of the [001]-orientation (right edge). The smaller spacing measured by TEM versus XRD (48 Å versus 56 Å, compare **a** and Fig. 2b) may be due to the over-focus condition used to achieve high contrast in TEM or electron-beam-induced shrinkage (normal to the substrate) which can occur in general for uncalcined, mesostructured materials. **b**, **c**, Two orientations of a cubic nanocomposite film prepared using 2.23% DA-EO_{10} surfactant. A highly ordered [100] orientation with unit-cell parameter at 108 Å, agreeing well with the XRD results. **c**, The corresponding [111] orientation with repeat distance of 62 Å. As for the corresponding XRD patterns, the cubic mesostructures revealed by TEM were quite comparable with and without the addition of co-surfactants (structure **1**, with $n = 3$ or 5, or structure **2**) needed to polymerize the blue or red forms of PDA within the cubic mesostructure. **d**, PDA/silica nanocomposite particles prepared using an aerosol-assisted evaporation-induced self-assembly technique[32]. The particle exhibits an ordered multi-lamellar exterior and a disordered worm-like mesostructured interior, consistent with a radially directed self-assembly process.

Figure 1 illustrates a postulated length-wise polymerization of surfactants within a cylindrical rod-like micelle to yield the blue form of PDA. Circumferential polymerization, although favoured on the basis of proximity of reactive DA moieties, would impose a high curvature on the PDA backbone because of the small pore size of the mesostructured host (2.5–3.0 nm in diameter, see Fig. B in the Supplementary Information). Although DA surfactants organized into ellipsoidal liposomes (40 nm × 15 nm) are known to polymerize in the blue and red forms[23] we questioned whether circumferential arrangements of DA surfactants (within spherical or cylindrical micelles) could polymerize with the proper 'ene'–'yne' conjugation to produce coloured materials. Molecular mechanics and dynamics calculations indicate that cyclic arrangements of up to 19 DA monomers around the periphery of the 3.0-nm-diameter pore are possible and that an energy-optimized 16-membered cyclic PDA oligomer can exhibit absorption behaviour consistent with the blue form of PDA (see Fig. 1d). Helical conformations[24] represent an alternative configuration that might satisfy DA proximity requirements without severely disrupting the conjugation. In general, nonlinear conformations may be needed for polymer propagation within these self-assembled nano-structured hosts. Such conformations are presumably rare or impossible for Langmuir monolayers and Langmuir–Blodgett films.

The PDA/silica nanocomposite films are optically transparent and mechanically robust. Modulus values measured by nanoindentation (3.50 ± 1.00 GPa) are compared to those of calcined mesoporous silica films that have been successfully integrated into microelectronic devices as low dielectric constant films (Y.L. and C.J.B., unpublished work). Nitrogen sorption experiments performed using a surface acoustic wave technique[25] show the nanocomposite films to be nonporous to nitrogen at −196 °C (Type II sorption isotherm, see Fig. B of the Supplementary Information), meaning that the PDA completely fills the pore channels and that the composite architecture may impart some degree of oxidation resistance (important for extension to other conjugated polymer nanocomposites).

The blue PDA/silica nanocomposites thus exhibit solvatochromic, thermochromic, and mechanochromic properties. When contacted with the series of polar solvents—2-propanol, acetone, ethanol, methanol and dimethylformamide—the films transform to the red, fluorescent form and the differential absorbance (A) at 645 nm ($A_{blue} - A_{red}$) scales linearly with the dielectric constant of the solvent: $A_{645\,nm} = 0.003$ (dielectric constant) − 0.005; for a correlation coefficient of 0.992 (see Fig. 4f), suggesting applications in sensing. We suggest that polar solvents diffuse within the polar, hydrophilic EO_n pendant side chains. The accompanying solvation stresses are transferred to the PDA backbone (evidence for solvation stresses are presented in Fig. A of the Supplementary Information), reducing its conjugation length, and therefore inducing the blue → red transformation[26] as understood by recent molecular mechanics simulations[27]. The solvatochromic behaviour shows very slow reversibility. Heating to temperatures in excess of 47 °C can also cause the blue → red transformation, and preliminary results have shown this thermochromic behaviour to be rapidly reversible (several seconds). This may arise from hydrogen-bonding interactions[26] of the pendant side chains with the silanol moieties

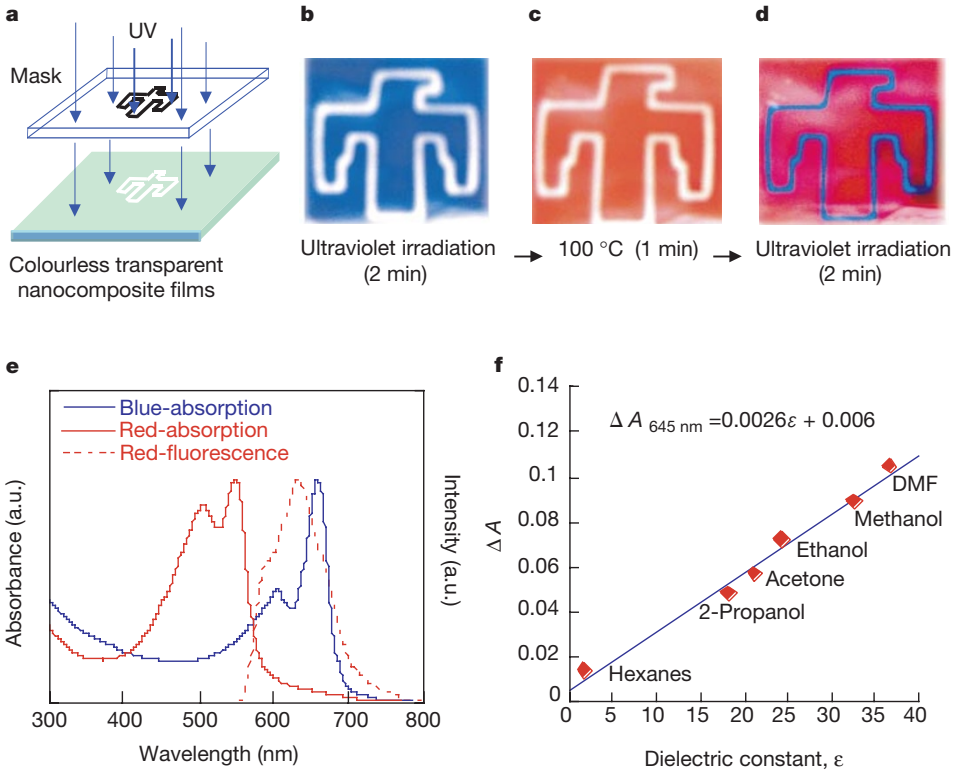

Figure 4 Patterned polymerization induced by ultraviolet irradiation and the thermochromic and solvatochromic transition of a hexagonal PDA/silica nanocomposite film. **a**, Schematic representation of the ultraviolet patterning procedure. **b**, Patterned blue/colourless film formed by ultraviolet irradiation for 2 min. **c**, Patterned red/colourless film formed by heating the film in **b** to 100 °C for 1 min. **d**, Patterned red/blue film formed by ultraviolet exposure of film in **c** for 2 min. **e**, Ultraviolet–visible spectra of the blue PDA/silica hexagonally ordered nanocomposite, the corresponding red film formed by heating at 100 °C, and the fluorescence emission spectrum of the red film (excited at 500 nm). Film formed from structure **1**, with $n = 5$. **f**, Differential absorbance at 645 nm resulting from the solvatochromic transition of blue PDA/silica nanocomposite films to the corresponding red films upon immersion of the blue films in the series of solvents: hexane, 2-propanol, acetone, ethanol, methanol, or dimethylformamide. Immersion times were 3 s followed by drying in nitrogen at room temperature. Without consideration of the nonpolar solvent, hexane, the regression equation is $A_{645\,nm} = 0.003$ (dielectric constant) −0.005, correlation coefficient = 0.992.

of the surrounding inorganic mesophase, supplying a restoring force and enabling recovery of the original side-chain orientation. Mechanical abrasion of the blue nanocomposite film causes local transformation to the red fluorescent form. Thus we envision mechanochromic barrier coatings that could sense excessive mechanical damage by changing from the blue form to the red fluorescent form.

The use of polymerizable surfactants as both structure-directing agents and monomers in the various evaporation-driven self-assembly schemes developed recently[28,29] represents a general, efficient route to the formation of robust and functional nanocomposites. Synthesis of surfactants with polymerizable thiophene, acetylene or phenylenevinylene groups should enable the self-assembly of conductive, conjugated polymer/silica nanocomposites in thin-film forms suitable for integration into devices. Conductive polymers confined within rod-like micellar channels of an electrical insulator conjure ideas of molecular wires. Unlike conduction measurements with two-dimensional films, such as bilayers[30] and monolayers[31], hexagonally ordered nanocomposite mesophases are nearly one-dimensional structures that could allow efficient conductivity along the channel direction. □

Methods

Precursor solutions were synthesized from tetraethylorthosilicate (TEOS, $Si(OC_2H_5)_4$), diacetylenic surfactants (structure **1** with $n = 3$, 4, 5, 10; structure **2**, or combinations thereof) and HCl catalyst prepared in a THF/water solvent. The final reactant mole ratios were 1 TEOS:31.4–57.9 THF:4.96 H_2O:0.013 HCl:0.06–1.41 DA surfactant. Films were prepared by casting, spin-coating at 2,000 r.p.m., or dip-coating at a rate of 40 cm min^{-1}. Polymerization of PDA to the blue form was done by ultraviolet exposure at 266 nm for times ranging from 30 s to 30 min. Subsequent transformation to the red form was accomplished by heating at 100 °C for times ranging from 30 s to 2 min or by exposure to a solvent.

Molecular simulations were performed using Cerius[2] and Polygraf software and the Burchart–Dreiding 2.21 force field. Ultraviolet–visible spectra of the PDA oligomers were calculated from the transition wavelengths and oscillator strengths obtained from INDO/S calculations on the terminated polymer backbone structure obtained from the molecular dynamics calculation.

Received 3 November 2000; accepted 6 February 2001.

1. Dagani, R. Putting the "nano" into composites. *Chem. Eng. News* **77,** 25–37 (1999).
2. Giannelis, E. Polymer layered silicate nanocomposites. *Adv. Mater.* **8,** 29–35 (1996).
3. Asefa, T., Yoshina-Ishii, C., MacLachlan, M. J. & Ozin, G. A. New nanocomposites: putting organic function "inside" the channel walls of periodic mesoporous silica. *J. Mater. Chem.* **10,** 1751–1755 (2000).
4. Smith, R. C., Fischer, W. M. & Gin, D. L. Ordered poly(*p*-phenylenevinylene) matrix nanocomposites via lyotropic liquid-crystalline monomers. *J. Am. Chem. Soc.* **119,** 4092–4093 (1997).
5. Sellinger, A. *et al.* Continuous self-assembly of organic-inorganic nanocomposite coatings that mimic nacre. *Nature* **394,** 256–260 (1998).
6. Moller, K., Bein, T. & Fischer, R. X. Entrapment of PMMA polymer strands in micro- and mesoporous materials. *Chem. Mater.* **10,** 1841–1852 (1998).
7. Nguyen, T.-Q., Wu, J., Doan, V., Schwartz, B. J. & Tolbert, S. H. Control of energy transfer in oriented conjugated polymer-mesoporous silica composites. *Science* **288,** 652–656 (2000).
8. Kleinfeld, E. R. & Ferguson, G. S. Stepwise formation of multilayered nanostructural films from macromolecular precursors. *Science* **265,** 370–373 (1994).
9. Keller, S. W., Kim, H.-N. & Mallouk, T. E. Layer-by-layer assembly of intercalation compounds and heterostructures on surfaces: Toward molecular "beaker" epitaxy. *J. Am. Chem. Soc.* **116,** 8817–8818 (1994).
10. Sasaki, D. Y., Carpick, R. W. & Burns, A. R. High molecular orientation in mono- and trilayer polydiacetylene films imaged by atomic force microscopy. *J. Colloid Interf. Sci.* **229,** 490–496 (2000).
11. Charych, D., Nagy, J., Spevak, W. & Bednarski, M. Direct colorimetric detection of a receptor-ligand interaction by a polymerized bilayer assembly. *Science* **261,** 585–588 (1993).
12. Cheng, Q. & Stevens, R. Charge-induced chromatic transition of amino acid-derivatized polydiacetylene liposomes. *Langmuir* **14,** 1974–1976 (1998).
13. Cheng, Q., Yamamoto, M. & Stevens, R. Amino acid terminated polydiacetylene lipid microstructures: morphology and chromatic transition. *Langmuir* **16,** 5333-5342 (2000).
14. Mazumdar, S. Prospects for the polymer nanoengineer. *Science* **288,** 630–631 (2000).
15. Lu, Y. F. *et al.* Continuous formation of supported cubic and hexagonal mesoporous films by sol–gel dip coating. *Nature* **389,** 364–368 (1997).
16. Israelachvili, J. N. *Intermolecular and Surface Forces* Ch. 17 (Academic, San Diego, 1992).
17. Monnier, A. *et al.* Cooperative formation of inorganic-organic interfaces in the synthesis of silicate mesostructures. *Science* **261,** 1299–1303 (1993).
18. Day, D. & Ringsdorf, H. Polymerization of diacetylene carbonic acid monolayers at the gas-water interface. *J. Polym. Sci. Polym. Lett. Edn* **16,** 205–210 (1978).
19. Gaines, G. L. (ed.) in *Insoluble Monolayers at Liquid-Gas Interfaces* 281–300 (John Wiley, New York, 1966).
20. Menzel, H., Mowery, M. D., Cai, M. & Evans, C. E. Vertical positioning of internal molecular scaffolding within a single molecular layer. *J. Phys. Chem. B* **102,** 9550–9556 (1998).
21. Collins, M. Optical-properties of poly-diacetylene monolayers. *J. Polym. Sci. B* **26,** 367–372 (1988).
22. Kuriyama, K., Kikuchi, H. & Kajiyama, T. Molecular packings-photopolymerization behavior relationship of diacetylene Langmuir-Blodgett films. *Langmuir* **12,** 6468–6472 (1996).
23. Spevak, W. *et al.* Polymerized liposomes containing *C*-glycosides of sialic acid: Potent inhibitors of influenza virus in vitro infectivity. *J. Am. Chem. Soc.* **115,** 1146–1147 (1993).
24. Frankel, D. A. & O'Brien, D. F. Supramolecular assemblies of diacetylenic aldonamides. *J. Am. Chem. Soc.* **113,** 7436–7437 (1991).
25. Frye, G. C., Ricco, A. J., Martin, S. J. & Brinker, C. J. in *Mater. Res. Soc.* (eds Brinker, C. J., Clark, D. E. & Ulrich, D. R.) 349–354 (Reno, Nevada, 1988).
26. Patel, G. N., Chance, R. R. & Witt. J. D. A planar-non-planar conformational transition in conjugated polymer solutions. *J. Chem. Phys.* **70,** 4387–4392 (1979).
27. Burns, A. R., Carpick, R. W., Sasaki, D. Y. & Shelnutt, J. A. Mechanochromism, shear force anisotropy, and molecular mechanics in polydiacetylene monolayers. *Tribol. Lett.* (in the press).
28. Fan, H. *et al.* Rapid prototyping of patterned functional nanostructures. *Nature* **405,** 56–60 (2000).
29. Brinker, C. J. Lu, Y., Sellinger, A. & Fan, H. Evaporation-induced self-assembly: nanostructures made easy. *Adv. Mater.* **11,** 579–585 (1999).
30. Day, D. R. & Lando, J. B. Conduction in polydiacetylene bilayers. *J. Appl. Polym. Sci.* **26,** 1605–1612 (1981).
31. Suzuoki, Y., Kimura, A. & Mizutani, T. in *Proc. 7th Int. Symp. Electrets* 850–855 (IEEE, New York, 1991).
32. Lu, Y. *et al.* Aerosol-assisted self-assembly of spherical, silica nanoparticles exhibiting hexagonal, cubic and vesicular mesophases. *Nature* **398,** 223–226 (1999).

Supplementary information is available from *Nature*'s World-Wide Website (http://www.nature.com) or as paper copy from the London editorial office of *Nature*.

Acknowledgements

We thank J. Curro and F. van Swol for technical discussions and T. Bucheit for the nano-indentation results. This work was supported by the US Department of Energy Basic Energy Sciences Program, the Sandia National Laboratories Laboratory-Directed Research and Development Program, the National Aeronautics and Space Administration, the UNM/NSF Center for Micro-engineered Materials, and the Defense Advanced Research Projects Agency Bio-Weapons Defense Program. TEM investigations were performed in the Department of Earth and Planetary Sciences at the University of New Mexico. Sandia is a multiprogram laboratory operated by Sandia Corporation, a Lockheed-Martin Company, for the US DOE.

Correspondence and requests for materials should be addressed to C.J.B. (e-mail: cjbrink@sandia.gov).

Early Oligocene initiation of North Atlantic Deep Water formation

Richard Davies*, Joseph Cartwright†, Jennifer Pike† & Charles Line*

** ExxonMobil International Limited, St Catherine's House, 2 Kingsway, PO Box 393, London WC2B 6WF, UK*
† Department of Earth Sciences, PO Box 914, Cardiff University, Cardiff CF10 3YE, UK

Dating the onset of deep-water flow between the Arctic and North Atlantic oceans is critical for modelling climate change in the Northern Hemisphere[1,2] and for explaining changes in global ocean circulation throughout the Cenozoic era[3] (from about 65 million years ago to the present). In the early Cenozoic era, exchange between these two ocean basins was inhibited by the Greenland–Scotland ridge[3,4], but a gateway through the Faeroe–Shetland basin has been hypothesized[3,5]. Previous estimates of the date marking the onset of deep-water circulation through this basin—on the basis of circumstantial evidence from neighbouring basins—have been contradictory[5–9], ranging from about 35 to 15 million years ago. Here we describe the newly discovered Southeast Faeroes drift, which extends for 120 km parallel to the basin axis. The onset of deposition in this drift has been dated to the early Oligocene epoch (~35 million years ago) from a petroleum exploration borehole. We show that the drift was deposited under a southerly flow regime, and conclude that the

Formation cross-sections of singlet and triplet excitons in π-conjugated polymers

M. Wohlgenannt*†, Kunj Tandon†‡, S. Mazumdar§, S. Ramasesha‡ & Z. V. Vardeny*

** Department of Physics, University of Utah, Salt Lake City, Utah 84112, USA*
‡ Solid State and Structural Chemistry Unit, Indian Institute of Science, Bangalore 560012, India
§ Department of Physics, University of Arizona, Tucson, Arizona 85721, USA
† These authors contributed equally to this work

Electroluminescence in organic light-emitting diodes arises from a charge-transfer reaction between the injected positive and negative charges by which they combine to form singlet excitons that subsequently decay radiatively. The quantum yield of this process (the number of photons generated per electron or hole injected) is often thought[1] to have a statistical upper limit of 25 per cent. This is based on the assumption that the formation cross-section of singlet excitons, σ_S, is approximately the same as that of any one of the three equivalent non-radiative triplet exciton states, σ_T; that is, $\sigma_S/\sigma_T \approx 1$. However, recent experimental[2] and theoretical[3] work suggests that σ_S/σ_T may be greater than 1. Here we report direct measurements of σ_S/σ_T for a large number of π-conjugated polymers and oligomers. We have found that there exists a strong systematic, but not monotonic, dependence of σ_S/σ_T on the optical gap of the organic materials. We present a detailed physical picture of the charge-transfer reaction for correlated π-electrons, and quantify this process using exact valence bond calculations. The calculated σ_S/σ_T reproduces the experimentally observed trend. The calculations also show that the strong dependence of σ_S/σ_T on the optical gap is a signature of the discrete excitonic energy spectrum, in which higher energy excitonic levels participate in the charge recombination process.

The charge transfer (CT) reaction between the injected spin-half positively and negatively charged polarons (P^+ and P^-) proceeds by an intermediate metastable encounter complex (EC). The EC is a superposition of the overall eigenstate $|I\rangle$ of the initial reactant species and the overall eigenstate $|F\rangle$ of the final products of the CT reaction. Following the formation of an EC, conformational changes along reaction coordinates occur, leading to the formation of $|F\rangle$. For large yields $|EC\rangle$ must have simultaneously large overlaps with both $|I\rangle$ and $|F\rangle$. Here $|I\rangle = |P^+\rangle|P^-\rangle$, $|F\rangle = |[S/T]\rangle + |G\rangle$, with $|P^\pm\rangle$ being the polaron eigenstates, $|[S/T]\rangle$ is either a neutral singlet or a neutral triplet excited state of one participant, and $|G\rangle$ is the ground state of the other participant. In the absence of electron correlation $|P^\pm\rangle$, $|[S/T]\rangle$ and $|G\rangle$ are all described by single configurations[4]. In particular, as the occupancies of the one-electron levels are the same for the singlet and triplet, $\sigma_S \approx \sigma_T$ for weak electron correlation.

The above description breaks down for intermediate electron correlations that are valid for π-conjugated polymers. First, single-configuration descriptions are no longer valid. The $|P^\pm\rangle$ are now superpositions of multiple configurations involving low (high) energy occupied (unoccupied) one-electron levels. Thus partial CT leads to multiple excited states of the EC supermolecule, each of which can decay to give the neutral states of the two components. Second, the correlated singlet exciton is necessarily ionic, whereas the correlated triplet exciton has a large covalent character[5]; there is also a substantial energy splitting between them[6–8]. For large exciton production, the sum of the overlaps of the different eigenstates $|EC_j\rangle$ with $|I\rangle$ and $|F\rangle$ must be large. Because the initial polaronic species P^+ and P^- are necessarily ionic, the dominant $|EC_j\rangle$ must also be ionic, and hence the most likely outcome of the CT reaction is the creation of product species, at least one of which is ionic. We conclude that $\sigma_S > \sigma_T$. Furthermore, the relative contributions of electron correlation and topology to the overall optical gap, which determine the ionicities of the ground and excited states, are strongly material-dependent; hence we expect σ_S/σ_T to be material-dependent from general considerations alone.

For systems which are light-emitting the quantum efficiency for electroluminescence (EL) is $\eta_{EL} = \eta_1\eta_2\eta_3$, where η_1 is the singlet emission quantum efficiency, η_2 is the fraction of the total number of excitons that are singlets, and η_3 is the probability that the injected electrons and holes find each other to form electron–hole pairs[3]. As both η_1 and $\eta_3 < 1$, it follows that $\eta_{EL} < \eta_2 = \eta_{max}$. Although $\sigma_S > \sigma_T$ by itself does not change the magnitude of η_2 from 1/4, in the presence of competing processes, faster rates will yield higher yields. One such competing process is the spin-lattice relaxation, which at room temperature is sufficiently fast that $\eta_{max} = \sigma_S/(\sigma_S + 3\sigma_T)$ (refs 3 and 9), rather than simply the statistical probability of obtaining one singlet exciton per three triplet excitons (see Supplementary Information). Thus the study of σ_S/σ_T in organic materials also provides information about η_{max} in organic light-emitting diodes (OLEDs).

We use continuous wave (CW) photoinduced absorption (PA) and photoinduced absorption detected magnetic resonance (PADMR) techniques (see Methods and ref. 10) to measure σ_S/σ_T in various π-conjugated polymer and oligomer thin films. For illustration, we choose the case of methylated laddertype poly-(*para*-phenylene) (mLPPP; see Fig. 1a, inset for its chemical structure[11]). In Fig. 1a we show the CW PA spectrum of mLPPP at 80 K. The PA bands labelled P_1 and P_2 are the spectral signatures

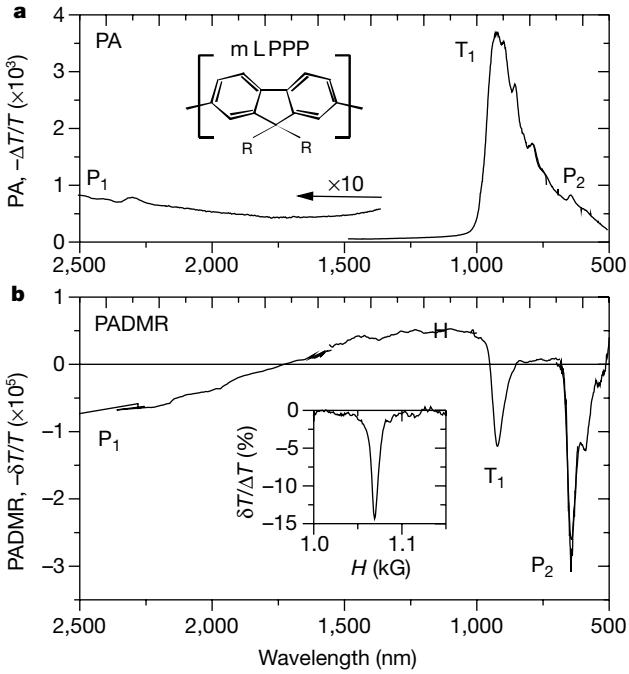

Figure 1 Spin-dependent recombination spectroscopy in π-conjugated polymers. For illustration the efficient blue emitter mLPPP (backbone is given in the inset to **a**) has been chosen. Its sharp spectral features make it ideal for spectroscopic studies[10]. **a**, The photoinduced absorption (PA) spectrum; **b**, the PA-detected magnetic resonance (PADMR) spectrum at constant magnetic field $H_{1/2} = 1.06$ kG. Both spectra **a** and **b** show two bands (P_1 and P_2) due to polarons, and one band (T_1) due to triplet absorption. The PA was measured at 80 K, the excitation was at the 457 nm line (~500 mW) of an Ar^+ laser; the PADMR spectrum was measured at 20 K. The inset in **b** shows the spin-half PADMR magnetic resonance at $H_{1/2} = 1.06$ kG detected at $\lambda = 2$ μm.

of polarons, whereas the PA band labelled T_1 corresponds to the triplet exciton[12]. Under CW illumination conditions CT reactions occur between neighbouring P^+ and P^-. The CT reaction rate R_P between spin parallel pairs (both ⇈ and ⇊), is proportional to $2\sigma_T$, whereas the reaction rate R_{AP} between spin antiparallel pairs (both ↑⇃ and ⇂↑), is proportional to $(\sigma_S + \sigma_T)$, where the proportionality constant is the same in both cases. $\sigma_S > \sigma_T$, so $R_{AP} > R_P$, and spin polarization of the recombining polaron pairs is built up over time, such that spin parallel pairs prevail under steady state illumination conditions[10].

Under saturated magnetic resonance conditions the Zeeman levels become equally populated, so that the pair densities with parallel and antiparallel spins are equal. Thus the effect of saturated magnetic resonance conditions is to increase the relative concentration of pairs with antiparallel spins whose reaction cross-section is larger, and as a consequence there is an overall decrease, δN, in the polaron population, N (see Fig. 1b inset). Figure 1b shows the wavelength-dependent PADMR spectrum of mLPPP where, in addition to a decrease in the polaron population (P_1 and P_2), a decrease in the triplet exciton population (T_1) is also measured. The negative triplet PADMR band confirms our statement that spin-half magnetic resonance decreases the population of neighbouring polaron pairs, especially those with parallel spins. The quantity $\delta T/\Delta T$ (see Methods) is then a direct measure of the fractional change in the overall photogenerated polaron population, $\delta N/N$.

The quantitative expression for $\delta N/N$ for distant pair kinetics under saturation conditions is given by[10]:

$$\delta N/N = -(R_P - R_{AP})^2/(R_P + R_{AP})^2 \quad (1)$$

From equation (1) and the proportionality relations above between R_P, R_{AP} and σ_S, σ_T, we obtain:

$$\frac{\sigma_S}{\sigma_T} = \frac{1 + 3|\delta T/\Delta T|^{1/2}}{1 - |\delta T/\Delta T|^{1/2}} \quad (2)$$

Thus the combination of PA and spin-half PADMR spectroscopy gives a direct measure of σ_S/σ_T. From Fig. 1b we get $\delta T/\Delta T \approx 14\%$ in mLPPP, corresponding to $\sigma_S/\sigma_T \approx 3.4$ from equation (2).

We performed similar PA and PADMR measurements for a large variety of π-conjugated polymers and oligomers. Our results are summarized in Fig. 2, where we plot the experimentally determined σ_S/σ_T as a function of the optical gap, E_g (see Supplementary Information for the experimental $\delta T/\Delta T$ values for each polymer). Individual $\sigma_S/\sigma_T > 1$ in all cases, giving $\eta_{max} > 25\%$; but there is a very large variation between the materials, which has never been seen before, to our knowledge. $\sigma_S/\sigma_T \approx 2.2$ in poly(phenylene-vinylene) (PPV), which corresponds to η_{max} of 42%, in excellent agreement with refs 2 and 9, works in which η_{max} was directly measured from OLED operation.

Although disorder, morphology and chain length distributions are all important, the systematic behaviour in Fig. 2 precludes any of these from being the dominant factor. The single biggest difference between the materials shown originates from the relative contribution of electron correlation and topology to the overall optical gap. Importantly, the lowest-energy excitations of all such systems can be mapped onto those of linear polyene chains with artificially large bond alternations[13]. We therefore theoretically examine the CT reaction between two charged polyene chains as a function of varying bond alternation.

Our goal is to calculate σ_S/σ_T for the CT reaction $|P^+\rangle + |P^-\rangle \rightarrow |[S/T]\rangle + |G\rangle$, for the case of antiparallel spins. We consider two parallel polyene chains separated by about 4 Å (Fig. 3 inset), described by the hamiltonian $H = H_1 + H_2 + H_{12}$, where H_k ($k = 1, 2$) describe the individual chains and H_{12} is the interaction between them. H_k is the single-chain Pariser–Parr–Pople hamiltonian[14,15], with the difference that the bond alternation parameter, δ, in the intrachain hopping integral[5], $t_\parallel(1 \pm \delta)$, is considered as a continuous variable. The interchain interaction is written as

$$H_{12} = \frac{1}{2}\sum_{i,j'} V_{i,j'}(n_i - 1)(n_{j'} - 1) - t_\perp \sum_{i\sigma}(c^\dagger_{i,\sigma}c_{i',\sigma} + \text{h.c.}) + \sum_{i,i',\sigma}[ii|ii'](n_i + n_{i'})(c^\dagger_{i,\sigma}c_{i',\sigma} + \text{h.c.}) \quad (3)$$

where h.c. is hermitian conjugate. Here i (j') are carbon atoms on chain 1 (2), $c^\dagger_{i,\sigma}$ creates a π-electron of spin σ on carbon atom i, n_i is the total number of electrons on carbon atom i, $V_{i,j'}$ is the interchain Coulomb interaction, i, i' are the nearest interchain neighbours with $t_\perp$ the corresponding hopping integral (see Fig. 3 inset), and $[ii,ii']$ is the bond-charge repulsion[16]. The second and the third terms in equation (3) promote interchain CT. Here $t_\parallel$ ($t_\perp$) is the intrachain (interchain) or parallel (perpendicular) hopping integral.

Exact calculations (see Methods of relative singlet and triplet yields were performed for pairs of ethylene, butadiene and hexatriene. Calculations for such small systems are not expected to give a quantitatively valid picture, which is not possible anyway, given the uncertainties in the parameters of H_{12}. Nevertheless, we believe that it is far more important to consider the full effects of electron correlation, rather than perform approximate calculations for longer polyenes and oligomers of the experimental systems that do not capture the many-body nature of $|P^\pm\rangle$, $|S\rangle$ and $|T\rangle$. In Fig. 3 we show the results of our model calculation for two hexatriene chains, where the calculated σ_S/σ_T ratio has been plotted versus the bond alternation parameter δ, for the specific case of $t_\perp = [ii|ii'] = 0.1$ eV. The calculated σ_S/σ_T in Fig. 3 exhibits three distinct peaks, with the first (relatively small) occurring at $\delta = 0$. Qualitatively similar results were also obtained with butadiene (see Supplementary Information).

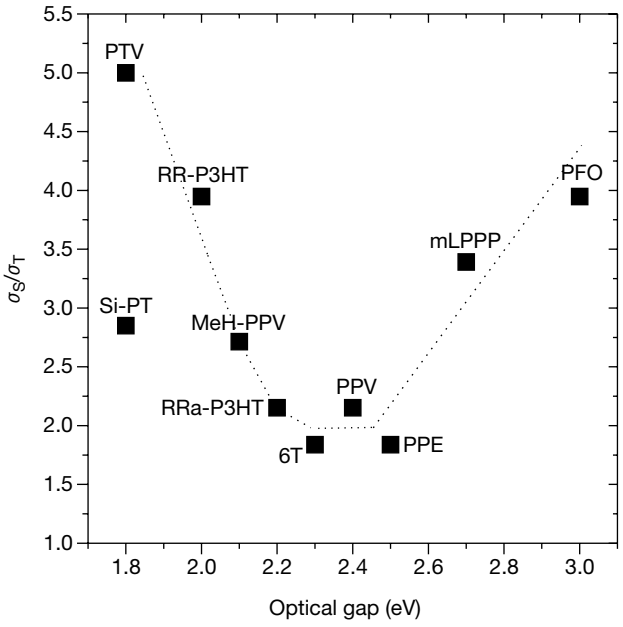

Figure 2 The experimentally determined σ_S/σ_T ratio for several π-conjugated polymers and oligomers as a function of the optical gap, E_g. σ_S/σ_T was evaluated using equation (2) from the measured $\delta T/\Delta T$ ratio for polarons in the PADMR and PA spectra, respectively. The dotted line is a guide to the eye. To ensure that δT were measured at saturated microwave absorption condition, we verified that the microwave field may be attenuated by 5 dB without reducing the observed $\delta T/\Delta T$ signals (see Supplementary Information). The values of $\delta T/\Delta T$ do not change with laser intensity or modulation frequency (see Supplementary Information) and are thus an intrinsic property of the individual polymer material.

The underlying mechanism for the occurrence of multiple peaks in Fig. 3 is as follows. For non-zero electron correlations the CT process need not lead to the lowest singlet or triplet exciton level. The correlated $|P^{\pm}\rangle$ wavefunctions, which consist of numerous configurations, change with increasing δ, and so both the individual $|EC_j\rangle$ and the specific eigenstate j that dominates the CT process evolve continuously. As a consequence of the changing character of $|P^{\pm}\rangle$, different n^1B_u exciton states dominate the CT yields at different δ, where n is the exciton quantum number. Furthermore, because the spectrum of our finite system is discrete, there exist regions of δ where neither of the two consecutive n^1B_u and $(n+1)^1B_u$ excitons give large yields. The three peaks in Fig. 3 at $\delta = 0$, 0.2 and 0.6 spectroscopically correspond to the 1^1B_u, the 2^1B_u and the 3^1B_u states, respectively (see Supplementary Information).

Similar effects also occur in the polymers (Fig. 2), where topological one-electron contributions to E_g increase from polyfluorene (PFO) to poly(thienylene vinylene) (PTV). Two aspects of the polymers allow direct comparison to our short-chain calculations. First, enhanced contribution of the topological gap to E_g can be simulated by increasing δ within effective linear-chain models[13]. Second, long-range Coulomb interactions in the Pariser–Part–Pople hamiltonian[14,15] give several excitons even in the long-chain limit[17]. Thus the qualitative effect of increased topological contribution to the optical gap is the same as increasing δ in our model calculation in Fig. 3, that is, the dominant CT product for large topological gap is a n^1B_u exciton state with n larger than 1. Experimentally, the initial ^1B_u state that is the product of the CT reaction in mLPPP and PFO has a quantum number that is larger than the initial ^1B_u state in the case of PTV and regio-regular poly(3-hexylthiophene) (RR-P3HT), with α-hexathiophene (6-HT), PPV and poly(phenylene-ethylene) (PPE) lying in a region of parameter space that corresponds to one of the valleys in Fig. 3. It is difficult to assign δ values to all systems in Fig. 2. Previous work has assigned $\delta \geqslant 0.2$ to PPV (ref. 13), and with moderate shifts of the peaks in Fig. 3 with chain length to lower δ (see Supplementary Information), the valley in σ_S/σ_T may well occur near $\delta \simeq 0.2$, with the next peak occurring at $\delta \approx 0.5$. We therefore conclude that the obtained systematic variation of the σ_S/σ_T shown in Fig. 2 is a distinct signature of the excitonic energy spectrum of the lowest-lying excited states in π-conjugated polymers.

We have thus discovered, to the best of our knowledge, a new experimental technique to determine the σ_S/σ_T ratio in π-conjugated polymers and oligomers using a spin-dependent recombination spectroscopy. The technique is very general, and may be used in other organic or inorganic materials that have long-lived charge excitations, particularly in determining the maximum EL yield in OLEDs made from the individual systems. Theoretically, our approach takes into account the full effects of electron correlation. The curious variation obtained in σ_S/σ_T with E_g is a novel electron correlation effect, that gives a new perspective on the electron–hole recombination in organic semiconductors. □

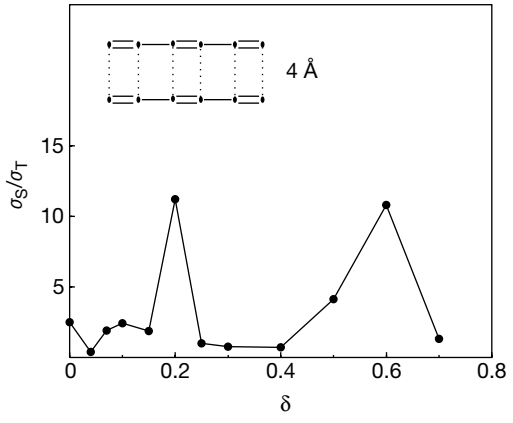

Figure 3 The calculated σ_S/σ_T for two parallel chains of hexatriene as a function of hypothetical bond alternation δ. The inset shows the actual arrangement of the chains chosen for the calculation.

Methods

The CW PA and spin-half PADMR techniques

The CW PA technique measures the excited state absorption spectrum of long-lived photoexcitations, such as triplet excitons and charged polarons. Two light beams are used; for the excitation beam we used an Ar^+ laser, the intensity of which was modulated with a chopper. We measured the pump-beam-induced changes, ΔT, in the probe beam (tungsten halogen lamp) transmission, T, using a monochromator and a combination of solid state detectors. The concentration, N, of the long-lived species is proportional to the corresponding PA intensity $(-\Delta T/T)$.

The PADMR technique measures the effect of spin-half magnetic resonance on the steady state population of photogenerated polarons and triplets. The experiment consists, in addition to the PA set-up, of a magnetic resonance part (microwave source and resonator, superconducting magnet). The sample is put inside the resonator and cooled by liquid helium. The PADMR set-up allows both PA and PADMR measurements under identical conditions. The change, δN, in the steady state population is proportional to the corresponding PADMR intensity $(-\delta T.T$, where δT is the resonant change in transmission). Experimentally the PADMR resonance is achieved by matching the energy splitting between the two Zeeman levels at magnetic field $H_{1/2}$ to the photon energy of an intense microwave field. For the 3-GHz microwave resonator used here, $H_{1/2}$ (corresponding to a g-value of 2) amounts to 1,060 G.

Computational technique

The approach for calculating σ_S/σ_T for the two charge chains is as follows. We use a time-dependent Schrödinger approach to calculate the time evolution of the initial state $\psi(0) = |P^+\rangle|P^-\rangle$, when operated by the overall hamiltonian H. The time evolution is done following a discretized procedure (see Supplementary Information), and after each evolution step, the evolved state $\psi(t)$ (which contains all the $|EC_j\rangle$) is projected onto the product of the eigenstates of the neutral systems. The yield for a given pair of product states is the overlap $|\langle\psi(t)|m,n\rangle|^2$, where $|m,n\rangle = |m\rangle \times |n\rangle$, with one of the two components $|m\rangle$ and $|n\rangle$ corresponding to $|[S/T]\rangle$ and the other to $|G\rangle$. The procedure was checked by performing the calculations first for the one-electron limit, where all yields are known.

Received 21 September; accepted 5 December 2000.

1. Friend, R. H. *et al.* Electroluminescence in conjugated polymers. *Nature* **397,** 121–128 (1999).
2. Cao, Y., Parker, I. D., Yu, G., Zhang, C. & Heeger, A. J. Improved quantum efficiency for electroluminescence in semiconducting polymers. *Nature* **397,** 414–417 (1999).
3. Shuai, Z., Beljonne, D., Silbey, R. J. & Bredas, J. L. Singlet and triplet exciton formation rates in conjugated polymer light-emitting diodes. *Phys. Rev. Lett.* **84,** 131–134 (2000).
4. Campbell, D. K., Bishop, A. R. & Fesser, K. Polarons in quasi-one-dimensional systems. *Phys. Rev. B* **26,** 6862–6874 (1982).
5. Soos, Z. G. & Ramasesha, S. Valence bond theory of linear Hubbard and Pariser-Parr-Pople models. *Phys. Rev. B* **29,** 5410–5422 (1984).
6. Lavrentiev, M. Yu., Barford, W., Martin, S. J., Daly, H. & Bursill, R. J. Theoretical investigation of the low-lying electronic structure of poly(p-phenylene vinylene). *Phys. Rev. B* **59,** 9987–9994 (1999).
7. Rohlfing, M. & Louie, S. G. Optical excitations in conjugated polymers. *Phys. Rev. Lett.* **82,** 1959–1962 (1999).
8. Monkman, A. P. *et al.* The triplet state of the ladder-type methyl-poly(p-phenylene) as seen by pulse radiolysis-energy transfer. *Chem. Phys. Lett.* **327,** 111–116 (2000).
9. Kim, J., Ho, P. K. H., Greenham, N. C. & Friend, R. H. Electroluminescence emission pattern of organic light-emitting diodes: Implications for device efficiency calculations. *J. Appl. Phys.* **88,** 1073–1081 (2000).
10. Vardeny, Z. V. & Wei, X. in *Handbook of Conducting Polymers II* (eds Skotheim, T. A., Elsenbaumer, R. L. & Reynolds, J. R.) 639–666 (Marcel Dekker, New York, 1997).
11. Graupner, W. *et al.* Direct observation of ultrafast field-induced charge generation in ladder-type poly(para-phenylene). *Phys. Rev. Lett.* **81,** 3259–3262 (1998).
12. Wohlgenannt, M., Graupner, W., Leising, G. & Vardeny, Z. V. Photogeneration and recombination processes of neutral and charged excitations in films of a ladder-type poly(para-phenylene). *Phys. Rev. B* **60,** 5321–5330 (1999).
13. Soos, Z. G., Ramasesha, S. & Galvão, D. S. Band to correlated crossover in alternating Hubbard and Pariser-Parr-Pople chains: Nature of the lowest singlet excitation of conjugated polymers. *Phys. Rev. Lett.* **71,** 1609–1612 (1993).
14. Pariser, R. & Parr, R. G. A semi-empirical theory of the electronic spectra and electronic structure of complex unsaturated molecules II. *J. Chem. Phys.* **21,** 767–776 (1953).
15. Pople, J. A. Electron interaction in unsaturated hydrocarbons. *Trans. Faraday Soc.* **49,** 1375–1385 (1953).
16. Campbell, D. K., Gammel, J. T. & Loh, E. Y. Bond-charge Coulomb repulsion in Peierls-Hubbard models. *Phys. Rev. B* **38,** 12043–12046 (1988).
17. Gallagher, F. & Mazumdar, S. Excitons and optical absorption in one-dimensional extended Hubbard models with short- and long-range interactions. *Phys. Rev. B* **56,** 15025–15039 (1997).

Supplementary information is available on *Nature*'s World-Wide Web site or as paper copy from the London editorial office of *Nature*.

Acknowledgements

We thank E.J.W. List for supplying the mLPPP polymer, and X.M. Jiang and E.J.W. List for their support in performing the experiments. The work at the University of Utah was supported in part by the DOE and the NSF. Work in Arizona was partially supported by the ONR through the MURI centre (CAMP) at the University of Arizona. Work in Bangalor was funded by CSIR, India.

Correspondence and requests for materials should be addressed to Z.V.V. (e-mail: val@physics.utah.edu).

Riverine export of aged terrestrial organic matter to the North Atlantic Ocean

Peter A. Raymond*† & James E. Bauer*

**School of Marine Science, College of William and Mary, Gloucester Point, Virginia 23062, USA*

† Present address: Marine Biological Laboratory, Ecosystems Center, Woods Hole, Massachusetts 02543, USA

Global riverine discharge of organic matter represents a substantial source of terrestrial dissolved and particulate organic carbon to the oceans[1,2]. This input from rivers is, by itself, more than large enough to account for the apparent steady-state replacement times of 4,00–6,000 yr for oceanic dissolved organic carbon[3–5]. But paradoxically, terrestrial organic matter, derived from land plants, is not detected in seawater and sediments in quantities that correspond to its inputs[6–8]. Here we present natural ^{14}C and ^{13}C data from four rivers that discharge to the western North Atlantic Ocean and find that these rivers are sources of old (^{14}C-depleted) and young (^{14}C-enriched) terrestrial dissolved organic carbon, and of predominantly old terrestrial particulate organic carbon. These findings contrast with limited earlier data[9] that suggested terrestrial organic matter transported by rivers might be generally enriched in ^{14}C from nuclear testing, and hence newly produced. We also find that much of the young dissolved organic carbon can be selectively degraded over the residence times of river and coastal waters, leaving an even older and more refractory component for oceanic export. Thus, pre-ageing and degradation may alter significantly the structure, distributions and quantities of terrestrial organic matter before its delivery to the oceans.

We sampled four rivers that discharge to the western North Atlantic Ocean: the Amazon (Brazil), Hudson (New York, USA), York (Virginia, USA) and Parker (Massachusetts, USA). The Amazon was sampled during base flow in 1991, and the three US rivers were sampled during moderate to high flow regimes from 1996 to 1998. The four sampled rivers range over four orders of magnitude in freshwater discharge (160,000, 375, 70 and 11 $m^3 s^{-1}$, respectively) and watershed size (7,050,000, 21,000, 4,350 and 609 km^2, respectively). All water samples were taken from tidal freshwater sites except the Parker River sample, which was taken from above a dam feeding the Parker estuary. We report radiocarbon (^{14}C) signatures for two operationally defined size fractions of organic matter: dissolved organic carbon (DOC; the fraction passing through a 0.7-μm glass-fibre filter) and particulate organic carbon (POC; the fraction collected on a 0.7-μm glass-fibre filter). Together these two size classes comprise the total organic carbon in these river waters. We also present for comparison data from four other western North Atlantic rivers[10] collected previously.

Mean DOC and POC concentrations for all rivers were 357 ± 280 μM and 95 ± 33 μM, respectively (Tables 1 and 2). The $\Delta^{14}C$ of DOC exported from these rivers was highly variable, ranging over 415‰ ($\Delta^{14}C$ is defined in Table 1.) The Hudson River DOC had the most depleted $\Delta^{14}C$ value at −158‰ (equivalent radiocarbon age of 1,384 years before present, yr BP), while the DOC from the Susquehanna and Rappahannock rivers was also low in $\Delta^{14}C$-DOC, with corresponding ages of 680 and 766 yr BP (Table 1). In contrast, the $\Delta^{14}C$ of DOC in the York, Parker, Potomac and Amazon rivers all contained 'bomb' ^{14}C (that is, $\Delta^{14}C > -50‰$), introduced by nuclear weapons testing in the 1950s and 1960s.

The corresponding $\Delta^{14}C$ values for POC (Table 2) were all significantly depleted compared to DOC (Table 1). The average $\Delta^{14}C$-POC values for the Amazon, Hudson, York and Parker rivers were −145, −437, −68 and −138‰ and had corresponding average radiocarbon ages of 1,258, 4,609, 690 and 1,210 yr BP, respectively; the greatest ages for POC from these four rivers were 1,258, 4,763, 1,690 and 1,696 yr BP, respectively (Table 2). This suggests that on average, the bulk POC discharged from these rivers was photosynthetically fixed several millennia ago, and a significant fraction of this POC aged on land and in river basins for hundreds to thousands of years. Very old riverine POC (>10,000 yr BP) has also been found in a subtropical mountainous river in Taiwan[11]. The average radiocarbon ages of POC in the present study were 1,260, 3,225, 690 and 1,210 years older than DOC in the Amazon, Hudson, York and Parker rivers, respectively (Tables 1 and 2). The $\Delta^{14}C$ values of Amazon DOC and POC were ~200‰ lower than values found further upriver in 1984 for dissolved humic substances and POC[9], and reflects a decrease in atmospheric $\Delta^{14}C$-CO_2 of 140‰ over the same period[12], spatial variation in POC sources[13], as well as our

Table 1 Concentrations and isotope data for riverine DOC

River	Date	DOC (μM)	$\Delta^{14}C$ (‰)	Radiocarbon age (yr BP)	$\delta^{13}C$ (‰)
Amazon	11/91	235	28±6	Modern	−28.0
Hudson	06/98	196	−158±7	1,384	−25.5
York	09/96	701	216±5	Modern	−28.8
	11/96	443	208±5	Modern	−27.9
	03/97	390	257±7	Modern	−28.0
	06/97	435	159±5	Modern	−28.0
Parker	06/98	986	109±6	Modern	−28.3
Potomac*	1972	364	+161	Modern	−30.9
Susquehanna*	1972	292	−81	680	ND
Rappahannock*	1973	125	−91	766	−31.9
James*	1973	167	+42	Modern	−28.0

Values of $\Delta^{14}C$ are expressed as the deviation in parts per thousand (‰) from the ^{14}C activity of nineteenth century wood. $\delta^{13}C$ values are expressed as $((R_{sample}/R_{standard}) - 1) \times 10^3$ in ‰, where $R = {}^{13}C/{}^{12}C$, and the standard is the Pee Dee Belemnite. DOC samples (100 ml of 0.7-μm-filtered river water) were oxidized to CO_2 by high-energy (2,400 W) ultraviolet (UV) irradiation for 2 h (refs 3, 5). The CO_2 samples were then converted to graphite and analysed for $\Delta^{14}C$ by accelerator mass spectrometry (AMS)[30]. All $\Delta^{14}C$ values were corrected for sample $\delta^{13}C$ (ref. 31). Errors (± 1σ) associated with $\Delta^{14}C$ AMS analyses averaged ±6‰ (±60 years for radiocarbon age), while those for $\delta^{13}C$ analyses averaged ±0.1‰. Concentrations of DOC were determined as part of the UV oxidation and CO_2 purification procedure, with quantification by a positive pressure (Baratron) gauge. The average error (± 1σ) for DOC concentrations determined by this method was ±1 μM. ND, not determined.
*Values from ref. 10, standard deviations not available.

20. Anton van der Merwe, P., Davis, S. J. & Dustin, M. L. Cytoskeletal polarization and redistribution of cell-surface molecules during T cell antigen recognition. *Semin. Immunol.* **12,** 5–21 (2000).
21. Cunningham, B. C. *et al.* Dimerization of the extracellular domain of the human growth hormone receptor by a single hormone molecule. *Science* **254,** 821–825 (1991).
22. Plotnikov, A. N., Schlessinger, J., Hubbard, S. R. & Mohammadi, M. Structural basis for FGF receptor dimerization and activation. *Cell* **98,** 641–650 (1999).
23. Wilson, I. A. & Jolliffe, L. K. The structure, organization, activation and plasticity of the erythropoietin receptor. *Curr. Opin. Struct. Biol.* **9,** 696–704 (1999).
24. Luo, R. Z. -T., Beniac, D. R., Fernandes, A., Yip, C. C. & Ottensmeyer, F. P. Quaternary structure of the insulin-insulin receptor complex. *Science* **285,** 1077–1080 (1999).
25. Otwinowski, Z. & Minor, W. Processing of X-ray diffraction data collected in oscillation mode. *Methods Enzymol.* **176,** 307–326 (1997).
26. Brunger, A. T. *et al.* Crystallography & NMR system: a new software suite for macromolecular structure determination. *Acta. Crystallogr. D* **54,** 905–921 (1998).
27. Jones, T. A., Cowan, S., Zou, J. Y. & Kjeldgaard, M. Improved methods for building protein models in electron density maps and the location of errors in these models. *Acta Crystallogr. A* **47,** 110–119 (1991).
28. Laskowski, R. A., MacArthur, M. W. & Thornton, J. M. Validation of protein models derived from experiment. *Curr. Opin. Struct. Biol.* **8,** 631–639 (1998).
29. Lawrence, M. C. & Colman, P. M. Shape complementarity at protein/protein interfaces. *J. Mol. Biol.* **234,** 946–950 (1993).
30. Evans, S. V. SETOR: hardware-lighted three-dimensional solid model representations of macromolecules. *J. Mol. Graph.* **11,** 134–138 (1993).
31. Barton, G. J. Protein multiple sequence alignment and flexible pattern matching. *Methods Enzymol.* **183,** 403–428 (1990).
32. Holm, L. & Sander, C. Dali: a network tool for protein structure comparison. *Trends Biochem. Sci.* **20,** 478–480 (1995).

Acknowledgements

We thank M. Scharff, P. Scherer, A. Davidson, A. Bresnick, T. DiLorenzo, A. Kalergis and M. Roden for comments. We also thank K. Rajashankar for assistance with data collection. This work was supported by grants from the National Institute of Allergies and Infectious Diseases. We acknowledge the support of the Albert Einstein Comprehensive Cancer Center.

Correspondence and requests for materials should be addressed to S.C.A. (e-mail: almo@aecom.yu.edu) or S.G.N. (e-mail: nathenso@aecom.yu.edu).

Crystal structure of the B7-1/CTLA-4 complex that inhibits human immune responses

Carin C. Stamper*, Yan Zhang*†, James F. Tobin*, David V. Erbe*, Shinji Ikemizu‡, Simon J. Davis§, Mark L. Stahl*, Jasbir Seehra*, William S. Somers* & Lidia Mosyak*

** Departments of Biological Chemistry and Musculoskeletal Sciences, Wyeth Research, 87 Cambridge Park Drive, Cambridge, Massachusetts 02140, USA*
‡ Division of Structural Biology, The Henry Wellcome Building for Genomic Medicine, The University of Oxford, Roosevelt Drive, Oxford OX3 7BN, UK
§ Nuffield Department of Clinical Medicine, The University of Oxford, John Radcliffe Hospital, Headington, Oxford OX3 9DU, UK

Optimal immune responses require both an antigen-specific and a co-stimulatory signal. The shared ligands B7-1 and B7-2 on antigen-presenting cells deliver the co-stimulatory signal through CD28 and CTLA-4 on T cells. Signalling through CD28 augments the T-cell response, whereas CTLA-4 signalling attenuates it. Numerous animal studies[1,2] and recent clinical trials[3,4] indicate that manipulating these interactions holds considerable promise for immunotherapy. With the consequences of these signals well established, and details of the downstream signalling events emerging[5–7], understanding the molecular nature of these extracellular interactions becomes crucial. Here we report the crystal structure of the human CTLA-4/B7-1 co-stimulatory complex at 3.0 Å resolution. In contrast to other interacting cell-surface molecules, the relatively small CTLA-4/B7-1 binding interface exhibits an unusually high degree of shape complementarity. CTLA-4 forms homodimers through a newly defined interface of highly conserved residues. In the crystal lattice, CTLA-4 and B7-1 pack in a strikingly periodic arrangement in which bivalent CTLA-4 homodimers bridge bivalent B7-1 homodimers. This zipper-like oligomerization provides the structural basis for forming unusually stable signalling complexes at the T-cell surface, underscoring the importance of potent inhibitory signalling in human immune responses.

The extracellular domains of human soluble (s) CTLA-4, residues 3–125 (SWISSPROT numbering), and sB7-1, residues 1–214, were expressed in Chinese hamster ovary (CHO) cells. The complex containing fully glycosylated sCTLA-4 and sB7-1 was crystallized in the space group $C222_1$. In the crystal lattice, sCTLA-4 and sB7-1 monomers each associate as non-crystallographic, roughly two-fold symmetric homodimers; single copies of each homodimer together form the asymmetric unit (Fig. 1a). The association of the four monomers in the asymmetric unit is driven by the interaction of three surfaces: the surface mediating sB7-1 homodimerization; the CTLA-4 homodimer interface; and the receptor–ligand binding interface.

The structures of the uncomplexed sCTLA-4 (refs 8, 9) and sB7-1

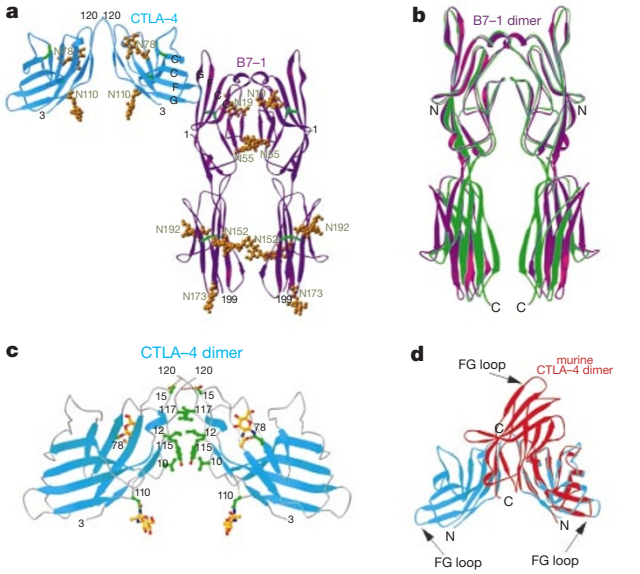

Figure 1 Structural comparison of sCTLA-4/sB7-1 complex with uncomplexed forms of sCTLA-4 and sB7-1. **a**, Ribbon diagram of the sCTLA-4/sB7-1 complex showing two sB7-1 (purple) and two sCTLA-4 (cyan) molecules in the asymmetric unit. Disulphide bonds (green) and sugar moieties (yellow) are also shown. β-sheets involved in the receptor–ligand interaction are labelled. Glycosylation sites on sCTLA-4 (Asn 78 and Asn 110) and on sB7-1 (Asn 19, Asn 55, Asn 152, Asn 173 and Asn 192) are all surface exposed. None of the ordered glycosides is involved in the receptor–ligand recognition. **b**, Superposition of the ligand-binding V-set domains of complexed (purple ribbons) and uncomplexed (cyan ribbons) forms of sB7-1. Apparent displacement of the membrane-proximal domains does not affect the interactions at the interdomain regions and is perhaps a result of differences in crystal packing contacts. **c**, Detailed view of the sCTLA-4 homodimer interface. Residues involved in hydrophobic interactions between the two monomers are shown in green. Two hydrogen bonds formed at the elbow of the homodimer are indicated as red dashed lines. Spatial proximity of the C termini (Glu 120) would enable a formation of disulphide bond between cysteines at positions 122. Asn 110 is the only strictly conserved glycosylation site in CTLA-4 and CD28. Located between the two monomers, *N*-glycans in these positions might stabilize the homodimer. **d**, Superposition of human sCTLA-4 dimer (cyan) on murine sCTLA-4 dimer (red). From this orientation, the contradiction between the two dimerization modes is evident. R.m.s. deviation between the two individual monomers is 1.5 Å for 114 Cα pairs. The FG loop of sCTLA-4 in the complex is displaced by 2.5 Å toward sB7-1. Figure prepared with RIBBONS[29].

† Present address: Pfizer Cambridge Discovery Technology Center, 620 Memorial Drive, Cambridge, Massachusetts 02139, USA.

(ref. 10) have shown that the two proteins comprise, respectively, a single V-set, and paired V-set and C1-set immunoglobulin superfamily (IgSF) domains. Overall, the sCTLA-4 and sB7-1 monomers do not show any significant conformational rearrangements on complex formation, apart from small local changes restricted to their binding sites. The glycosylated sB7-1 homodimer seen in the crystals of the complex is essentially identical to that observed in crystals of deglycosylated sB7-1 (ref. 10): the monomer–monomer interface is the same size (570 Å^2 per monomer; calculated using the program SURFACE[11]; probe radius 1.4 Å) and involves the same residues. When the V-set domains of the two sB7-1 homodimers are superimposed (Fig. 1b), the membrane-proximal C1-set domains are displaced by only 3 Å. Similar variation has been observed in individual crystals of sB7-1 (S.I. *et al.*, unpublished data), suggesting that these differences are more likely to result from variability in sB7-1 self-association than from the effects of ligand binding. sB7-1 homodimerization has been confirmed in solution using analytical ultracentrifugation methods[10].

Although the structure of the sCTLA-4 monomer is very similar to that of the murine sCTLA-4 monomer[8], the human and murine[8] sCTLA-4 homodimers observed in the two lattices are very different (Fig. 1c, d). Of the two structures, we consider that the sCTLA-4 homodimer present in the crystals of the complex represents the more plausible model for native CTLA-4. First, all of the interacting residues are strictly conserved, in contrast to the conservation of only four of the ten residues forming the murine dimer interface[8]. Second, the human sCTLA-4 homodimer is not precluded by glycosylation. If used as in human CTLA-4 (ref. 12), an *N*-linked glycan at the conserved Asn 78 glycosylation site would prevent murine-like homodimerization in all species. Third, the human homodimer allows co-ligation of sB7-1 molecules around an axis orthogonal to the membrane, maintaining the ~140 Å intermembrane distance thought to be a critical feature of the immunological synapse[5]. Last, the interchain disulphide bond will more readily form in the human sCTLA-4 homodimer. The 7.7 Å spacing between the Cα atoms of the last visible residue in each monomer (Pro 119) is more likely to be bridged by the three additional residues and by the disulphide bond in the human sCTLA-4 dimer than is the equivalent 30.1 Å distance in the murine structure. Consequently, the murine model for CTLA-4 dimerization and signalling proposed previously[8] is most probably not relevant to the formation of co-stimulatory complexes.

The human sCTLA-4 monomers interact through residues in the A and G β-strands (Val 10, Leu 12, Ser 15, Tyr 115, Ile 117, Glu 120), burying only 460 Å^2 of surface[11] per monomer. The interface is essentially hydrophobic except for reciprocal, interchain hydrogen bonds between the side chain of Ser 15 and the main-chain nitrogen of Glu 120 at the elbow of the homodimer (Fig. 1c). This weak interaction might explain why, in the absence of the interchain disulphide (Cys–Cys 122), sCTLA-4 is monomeric in solution (ref. 9; and Y.Z. and M.S., unpublished data). The amino acids mediating CTLA-4 dimerization are not conserved in CD28; however, the equivalent residues exhibit the same overall hydrophobicity, implying that CD28 might form similar homodimers.

Differences noted[8] between the murine structure and the human sCTLA-4 structure determined by NMR methods[9] are also seen in the complex crystals. In particular, the V-set domain has C″DEBA:GFCC′ rather than DEBA:GFCC′C″ topology, and the three consecutive prolines in the FG loop, MY^{101}PPP^{103}Y, adopt the *cis–trans–cis* rather than *trans–trans–cis* conformation seen in the NMR structure[9]. This has important implications for B7-1 binding (see below).

Mutational data have implicated the membrane-proximal domain of B7-1 in interactions with CTLA-4 and CD28 (ref. 13), but these effects must have been indirect as sCTLA-4 only contacts residues of the sB7-1 V-set domain. Receptor–ligand binding occurs through the GFCC′ face of the sCTLA-4 and sB7-1 V-set domains, with a roughly 90° angle between the interacting β-sheets (Fig. 2a). In this orientation, the FG, BC and C′C″ loops of sCTLA-4 extend across the base of the sB7-1 five-stranded β-sheet, burying a total of 1,255 Å^2 of solvent-accessible surface[11] (600 Å^2 from sB7-1 and 655 A^2 from sCTLA-4). These values are at the low end of the range for protein–protein binding sites (600–900 Å^2)[14].

Orthogonal binding mediated by the GFCC′C″ face of the V-set IgSF domains of cell-surface molecules was first seen in rat and human sCD2 crystal contacts[15,16], and subsequently in the native complex of sCD2 and sLFA-3 (ref. 17) and in crystals of the coxsackie virus and adenovirus receptor[18]. It seems likely that this orthogonal binding mode will be a recurrent theme of V-set interactions. There is no compelling reason why such orthogonal interactions should have arisen through convergent evolution, but it is possible that these complexes bear the imprint of primordial IgSF interactions.

Interatomic contacts (85 total; van der Waals radius 3.9 Å) are made between 13 residues of CTLA-4 residues and 13 residues of

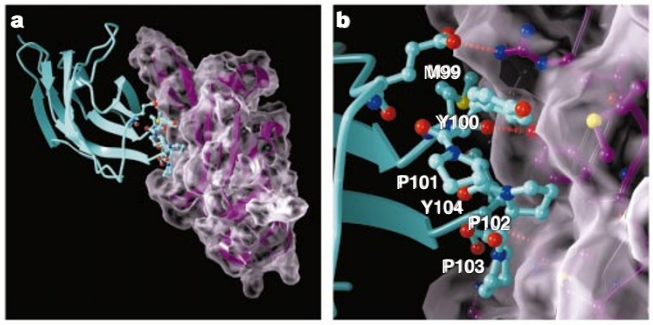

Figure 2 Overview of receptor–ligand interactions. **a**, Ribbon diagram showing orthogonal interaction between sCTLA-4 (cyan) and sB7-1 (purple) monomers. Also shown is the molecular surface representation (white transparent) of the ligand-binding domain of sB7-1 to emphasize the high geometric match between the two interacting surfaces. **b**, Direct receptor–ligand contacts. The ^{99}MYPPPY^{104} loop of sCTLA-4 is buried in a shallow depression of the sB7-1 GFCC′ surface. Colour coding is as in **a**. Three out of five hydrogen bonds formed across the β-sheets of the interacting domains are depicted as red dashed lines. Several other side chains on CTLA-4 and B7-1 (not shown) may contribute to the binding through appreciable, but not direct, contacts formed on the periphery of the binding interface. Figure prepared with BobScript[30].

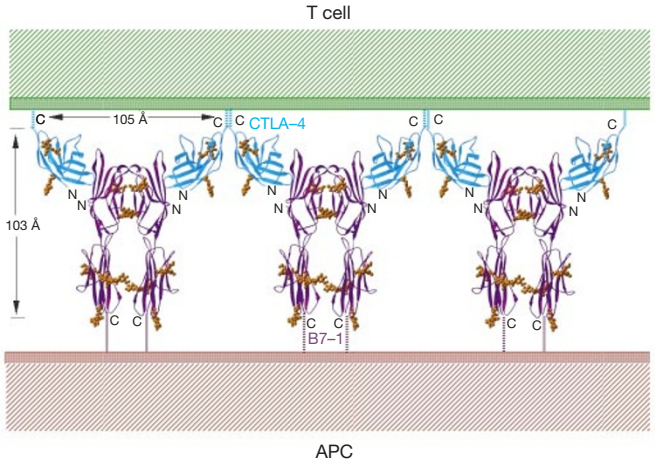

Figure 3 Molecular association of sCTLA-4 and sB7-1 in the crystal lattice. Shown are 'skewed zipper' arrays in which sCTLA-4/sB7-1 complexes would be evenly spaced along membrane surfaces with a separation of 105 Å. In the perpendicular direction, across membranes, ligated receptors would span 140 Å. Geometrically, sugar chains attached at Asn 173 on B7-1 (bottom) are close to the cell membrane, implying their potential involvement in interaction with the membrane, perhaps by stabilizing the orientation of the B7-1 dimers. APC, antigen-presenting cell. Figure prepared with RIBBONS[29].

B7-1. Most of these are hydrophobic contacts, but there are also five hydrogen bonds. The FG loop of sCTLA-4, which contains the hydrophobic ^{99}MYPPPYY^{105} sequence that is strictly conserved in CTLA-4 and CD28, dominates the interaction and contributes 400 Å^2 of protein surface[11] to the binding interface (Fig. 2b). The FG loop makes hydrophobic contacts with a largely nonpolar surface of sB7-1 consisting of Tyr 31, Met 38, Thr 41, Met 43, Val 83, Leu 85, Ala 91, Phe 92 and Leu 97.

Mutations of the two central residues, Tyr 31 and Met 38, disrupt B7-1 binding to CTLA-4 and CD28 (ref. 13); the other residues forming this surface have not been tested. Five hydrogen bonds, including one between the charged residues Glu 33 on sCTLA-4 and Arg 29 on sB7-1 are likely to contribute to the specificity of binding (Fig. 2b). All residues in the ^{99}MYPPPYY^{105} sequence, except Pro 101, are in direct contact with sB7-1, and all alanine substitutions of these residues, including Pro 101, reduce or abolish binding to B7-1 (ref. 9). Analysis of the complex structure indicates that the crucial role of Pro 101 is to initiate the *cis–trans–cis* main-chain conformation of the FG loop, directing Tyr 100, Pro 102, Pro 103 and Tyr 104 towards interactions with sB7-1. At the core of the interface, Pro 102 of CTLA-4 and Tyr 31 of B7-1 participate in a stacking interaction (Figs 2b, 4) that is likely to be conserved both across species and in interactions involving CD28 and B7-2 (in B7-2 Tyr 31 is replaced by phenylalanine).

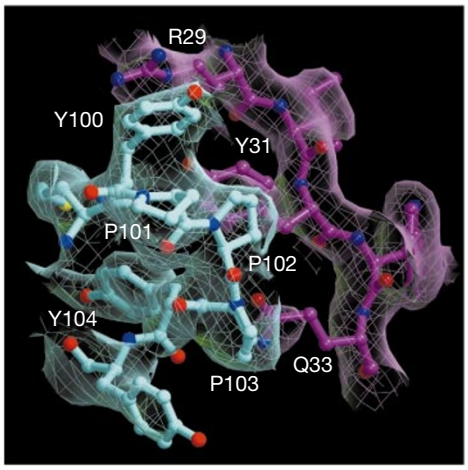

Figure 4 A 3 Å resolution electron-density map in the region of the receptor–ligand binding site. Electron density is from an annealed omit map calculated using the $3F_{obs} - 2F_{obs}$ amplitudes and model phases, with the CTLA-4 atoms excluded from the refinement and all calculations. The map is contoured at 1σ level. Colour coding is as in Figs 1 and 2.

Table 1 Statistics for data collection and refinement

Data collection		
Resolution range (Å)	20–3.0	3.11–3.0
Completeness (%)	99.2	94.1
Total observations	209,381	–
Unique reflections	38,815	3,636
Average $I/\sigma(I)$	19.1	3.0
R_{sym}*(%)	6.7	35.1
Model refinement		
Maximum resolution (Å)	3.0	
Number of reflections (free)	$F_{obs} > 2\sigma$	$F_{obs} > 0\sigma$
	31,410 (1,887)	35,465
R_{work}/R_{free} †(%)	23.1/25.9	25.3/28.2
r.m.s. deviations		
Bonds (Å)	0.010	
Angles (°)	1.48	

*$R_{sym} = \Sigma|I_h - \langle I_h\rangle|/\Sigma I_h$, where $\langle I_h\rangle$ is the average intensity over symmetry equivalents. Numbers in the second column reflect statistics for the last resolution shell.
†$R_{work} = \Sigma||F_{obs}| - |F_{calc}||/\Sigma|F_{obs}|$, R_{free} is equivalent to R_{work}, but calculated for a randomly chosen 6% of reflections omitted from the refinement process.

Accordingly, the two binding surfaces exhibit a very high degree of shape complementarity. An algorithm[19] measuring the degree of geometric fit between two protein surfaces gives scores of 0.74–0.77 for the sCTLA-4/sB7-1 binding interface. This value is similar to those for constitutive oligomeric proteins (0.7–0.76) and much higher than scores for protein antigen–antibody interfaces (0.64–0.68) or interacting cell-surface molecules (0.45–0.58; ref. 17 and references therein). This degree of complementarity accounts for the enthalpy-driven nature of binding (R. O'Brien *et al.*, personal communication), whereas the small interacting surfaces and slightly unfavourable entropy explain the very fast binding kinetics[12].

In the crystal lattice, the sCTLA-4 and sB7-1 homodimers pack together to form a periodic arrangement in which bivalent sCTLA-4 homodimers bridge bivalent sB7-1 homodimers (Fig. 3). The sB7-1 and shorter CTLA-4 homodimers associate orthogonally, thus generating a 'skewed zipper' arrangement. It has long been clear that CTLA-4 exists as a constitutive, bivalent homodimer, and the affinity of sB7-1 self-association (dissociation constant, K_d = 20–50 μM) indicates that B7-1 is also likely to exist as a dimer at the cell surface, albeit in dynamic monomer–dimer equilibrium[10]. We therefore expect oligomeric arrays that are similar, if not identical, to those seen in the crystals to form at the membrane interface between T cells and antigen-presenting cells.

Including the 'stalk' regions, the extracellular domains of the ligated receptors are expected to span a distance of ~140 Å between the opposing cell membranes, a distance compatible with that required by T-cell receptor (TCR)–MHC, natural killer cell inhibitory receptor (KIR)–MHC or CD2–CD58 intercellular interactions[5,17,20,21]. Overall, this arrangement is reminiscent of the 'cell-adhesion zipper' observed in the crystals of cadherins, which is thought to be a fundamental feature in adhesive interactions between cells expressing these molecules[22].

As far as is generally known, cell-surface molecules bind their ligands monovalently and with very low (micromolar) affinities[23]. The submicromolar affinity of B7-1 for CTLA-4 (K_d = 0.2–0.4 μM; ref. 12) is thus unusually high for interacting cell-surface molecules. Our structural analysis of the complex implies that potent B7-mediated inhibitory signalling is not based exclusively on the stability of association between individual homodimers, but rather that the counter-receptor oligomeric arrays will also strengthen the interaction between the opposing cells. The combination of sub-micromolar affinity and oligomeric, high-avidity binding is, to our knowledge, unique to CTLA-4/B7-1 interactions.

The amplification and attenuation of TCR signalling occurs in a specialized contact area on the cell surface, termed the immunological synapse[5,6], through the recruitment of receptors and their signalling complexes that effect the phosphorylation state of the TCR (ref.7). Notably, inhibition of TCR signalling by CTLA-4 has been seen only to occur when both signals are delivered by the same cell surface[24]; however, other data suggest that the regulatory signals delivered by CD28 and CTLA-4 may not be strictly cell autonomous[25]. Regardless of the precise nature of the signals and mechanisms involved, it now seems that the inhibition of immune responses by CTLA-4 requires the formation of unusually stable complexes, the structure of which is revealed by the crystals of sCTLA-4/sB7-1. Whether such stable complexes are required for the efficient use of low-abundance CTLA-4 molecules at the T-cell surface, or enhance the potency of inhibitory CTLA-4 signalling by concentrating key effector molecules such as the phosphatase SHP-2 (ref. 7) under the immunological synapse, or both, remains to be established. □

Methods

Production and purification of B7-1 and CTLA-4

Constructs encoding the extracellular portions of human CTLA-4 or B7-1 were fused to an enterokinase cleavage sequence (DYKDDDDK) followed by the IgG1 CH2–CH3 domains, and expressed in CHO cells. In addition, the cysteine at position 122 of CTLA-4

was mutated to serine. These were recovered from conditioned medium by protein-A chromatography, cleaved with enterokinase, further purified and confirmed to be monomeric by gel-filtration chromatography as described[26]. Appropriate binding characteristics for each protein were confirmed by surface plasmon resonance (Biacore) analysis and found to be consistent with published values[12]. For CTLA-4, the final cleaved protein comprised residues 3–125 (with the C122S mutation) followed by the octa-peptide DYKDDDDK at the carboxy terminus. For B7-1, the cleaved protein consisted of residues 1–214 with the DYKDDDDK octa-peptide again forming the C terminus.

Crystallization and data collection

The B7-1/CTLA4 complex was formed by incubating a 1:1.5 molar ratio of B7-1 and CTLA4 and purified using a TSK-3000SW size exclusion column (TosoHaas). The purified complex was buffer exchanged and concentrated to 10 mg ml^{-1} in 20 mM Tris-HCl, pH 8.0. Crystals were grown at 18 °C by the hanging drop method by combining 2 μl of protein solution with 2 μl of 14% PEG 8000, 200 mM magnesium acetate and 100 mM cacodylate, pH 6.3, and equilibrated against 1 ml of the same solution. Crystals appeared in 5 days and were soaked in 16% PEG 8000, 200 mM magnesium acetate, 20 mM Tris-HCl pH 8.0, 100 mM cacodylate, pH 6.3, 20% ethylene glycol for about 1 min before plunging into liquid nitrogen. Crystals belong to space group $C222_1$ with unit-cell dimensions a = 88.5, b = 183.4, c = 230.8 Å and a calculated solvent content of 58% for two B7-1 and two CTLA-4 molecules per asymmetric unit (adding 82,000 (82K) of glycosylation estimated from SDS–PAGE gel mobility). The 3.0 Å resolution data were collected from a single crystal at 100K at Beamline 5.0.2 at the Advanced Light Source using a Quantum 4 CCD. 725 0.2° rotation images were collected and reduced with HKL2000 (ref. 27) giving statistics outlined in Table 1.

Structure determination and refinement

The structure was solved by molecular replacement in CNS[28] using the crystallographic dimer observed in the human B7-1 structure as the search model[10]. After rigid body refinement of each B7-1 domain the R factor was 55.3%. Initial electron-density maps phased with B7-1 alone showed clear electron density for the two CTLA-4 molecules . The model of murine CTLA-4 monomer (PBD accession number 1dqt) was placed into electron density and was manually rebuilt in QUANTA (Molecular Simulations) to reflect the sequence of human CTLA-4. Non-conserved amino-acid residues and loop regions of CTLA-4 and B7-1, as well as sugar moieties, were entirely built into electron density. A composite annealed omit map was calculated to check the conformation of CTLA-4 and B7-1 loop regions. All refinement procedures were done in CNS and used data from 20.0–3.0 Å. A 2σ cut-off was applied during the refinement because of the anisotropy of the data. Six per cent of the reflections were randomly selected for generation of the R_{free} data set (see Table 1). The anisotropy of the data was corrected for also using CNS.

Tight non-crystallographic symmetry restraints were gradually relaxed during the refinement process resulting in a final model with R_{work} of 23.2% and R_{free} of 25.9%. Continuous electron density was seen for sugar moieties at four N-linked carbohydrate sites on CTLA-4 dimer (Asn 78 and Asn 110) and at ten glycosylation sites on B7-1 dimer (Asn 19, Asn 55, Asn 152, Asn 173 and Asn 192). No saccharides could be modelled at six other expected glycosylation sites on B7-1 (Asn 64, Asn 177 and Asn 198). The final model contains two B7-1 molecules (residues A1–A199 and B1–B199), two CTLA-4 molecules (residues C3–C120 and D3–D120), 20 monosaccharides and shows reasonable geometry: 98.9% of non-glycine φ and ψ angles lie in the allowed regions of the Ramachandran plot (77.6% in the most favoured regions and 21.4% in additionally allowed regions); six amino-acid residues (1.1%) have disallowed angles.

Received 27 December 2000; accepted 9 February 2001.

1. Lenschow, D. J., Walunas, T. L. & Bluestone, J. A. CD28/B7 system of T cell costimulation. *Annu. Rev. Immunol.* **14,** 233–258 (1996).
2. Greenfield, E. A., Nguyen, K. A. & Kuchroo, V. K. CD28/B7 costimulation: a review. *Crit. Rev. Immunol.* **18,** 389–418 (1998).
3. Guinan, E. C. *et al.* Transplantation of anergic histoincompatible bone marrow allografts. *N. Engl. J. Med.* **340,** 1704–1714 (1999).
4. Abrams, J. R. *et al.* Blockade of T lymphocyte costimulation with cytotoxic T lymphocyte-associated antigen 4-immunoglobulin (CTLA4Ig) reverses the cellular pathology of psoriatic plaques, including the activation of keratinocytes, dendritic cells, and endothelial cells. *J. Exp. Med.* **192,** 681–694 (2000).
5. van der Merwe, P. A. Davis, S. J., Shaw, A. S. & Dustin, M. L. Cytoskeletal polarization and redistribution of cell-surface molecules during T cell antigen recognition. *Semin. Immunol.* **12,** 5–21 (2000).
6. Grakoui, A. *et al.* The immunological synapse: a molecular machine controlling T cell activation. *Science* **285,** 221–227 (1999).
7. Lee, K.-M. *et al.* Molecular basis of T cell inactivation by CTLA-4. *Science* **282,** 2263–2266 (1998).
8. Ostrov, D. A., Shi, W., Schwartz, J.-C. D., Almo, S. C. & Nathenson, S. G. Structure of murine CTLA4 and its role in modulating T cell responsiveness. *Science* **290,** 816–819 (2000).
9. Metzler, W. J. *et al.* Solution structure of human CTLA4 and delineation of a CD80/CD86 binding site conserved in CD28. *Nature Struct. Biol.* **4,** 527–531 (1997).
10. Ikemizu, S. *et al.* Structure and dimerization of a soluble form of B7-1. *Immunity* **12,** 51–60 (2000).
11. Collaborative computational project No. 4. The CCP4 suite: Programs for protein crystallography. *Acta Crystallogr. D* **50,** 760–776 (1994).
12. van der Merwe, P. A., Bodian, D. L., Daenke, S., Linsley, P. & Davis, S. J. CD80 (B7-1) binds both CD28 and CTLA-4 with a low affinity and very fast kinetics. *J. Exp. Med.* **185,** 393–403 (1997).
13. Peach, R. J. *et al.* Both extracellular immunoglobulin-like domains of CD80 contain residues critical for binding T cell surface receptors CTLA-4 and CD28. *J. Biol. Chem.* **8,** 21181–21187 (1995).
14. Janin, J. & Chothia, C. The structure of protein-protein recognition sites. *J. Biol. Chem.* **265,** 16027–16030 (1990).
15. Jones, E. Y., Davis, S. J., Williams, A. F., Harlos, K. & Stuart, D. I. Crystal structure at 2. 8 Å resolution of a soluble form of the cell adhesion molecule CD2. *Nature* **360,** 232–239 (1992).
16. Bodian, D. L., Jones, E. Y., Harlos, K., Stuart, D. I. & Davis, S. J. Crystal structure of the extracellular region of the human cell adhesion molecule CD2 at 2.5 Å resolution. *Structure* **15,** 755–766 (1994).
17. Wang, J.-h. *et al.* Structure of a heterophilic adhesion complex between the human CD2 and CD58 (LFA-3) counterreceptors. *Cell* **7,** 791–803 (1999).
18. van Raaij, M. J., Chouin, E., van der Zandt, H., Bergelson, J. M. & Cusack, S. Dimeric structure of the coxsackievirus and adenovirus receptor D1 domain at 1. 7 Å resolution. *Struct. Fold Des.* **8,** 1147–1155 (2000).
19. Lawrence, M. C. & Colman, P. M. Shape complementarity at protein/protein interfaces. *J. Mol. Biol.* **234,** 946–950 (1993).
20. Garboczi, D. N. *et al.* Structure of the complex between human T-cell receptor, viral peptide and HLA-A2. *Nature* **384,** 134–141 (1996).
21. Boyington, J. C., Motyka, S. A, Schuck, P., Brooks A. G. & Sun, P. D. Crystal structure of an NK cell immunoglobulin-like receptor in complex with its class I MHC ligand. *Nature* **405,** 537–543 (2000).
22. Shapiro, L. *et al.* Structural basis of cell–cell adhesion by cadherins. *Nature* **374,** 327–337 (1995).
23. Davis, S. J., Ikemizu, S., Wild, M. K. & van der Merwe, P. A. CD2 and the nature of protein interactions mediating cell-cell recognition. *Immunol. Rev.* **163,** 217–236 (1998).
24. Griffin, M. D. *et al.* Blockade of T cell activation using a surface-linked single-chain antibody to CTLA-4 (CD152). *J. Immunol.* **164,** 4433–4442 (2000).
25. Bachmann, M. F., Kohler, G., Ecabert, B., Mak, T. W. & Kopf, M. Lymphoproliferative disease in the absence of CTLA-4 is not T cell autonomous. *J. Immunol.* **163,** 1128–1131 (1999).
26. Somers, W. S., Tang, J., Shaw, G. D. & Camphausen, R. T. Insights into the molecular basis of leukocyte tethering and rolling revealed by structures of P- and E-selectin bound to sLex and PSGL-1. *Cell* **103,** 467–479 (2000).
27. Otwinowski, Z. & Minor, W. Processing of X-ray diffraction data collected in oscillation mode. *Methods Enzymol.* **276,** 307–326 (1997).
28. Brunger, A. T. *et al.* Crystallography and NMR system (CNS): a new software suite for macro-molecular structure determination. *Acta Crystallogr. D* **54,** 905–921 (1998).
29. Carson, M. Ribbons 2.0. *J. Appl. Crystallogr.* **24,** 958–961 (1991).
30. Esnouf, R. M. An extensively modified version of Molscript that includes enhanced colouring capabilities. *J. Mol. Graph.* **15,** 132–134 (1997).

Acknowledgements

We thank R. Zollner and his colleagues for large scale cell culture, and D. I. Stuart and E. Y. Jones for helpful comments. We also thank the staff at Advanced Light Source for assistance with data collection. S.I. and S.J.D. are supported by the Wellcome Trust and the Human Frontier Science Programme.

Correspondence and requests for materials should be addressed to W.S.S. (e-mail: wsomers@genetics.com) or L.M (e-mail: lmosyak@genetics.com). The coordinates have been deposited in the Protein Data Bank. The accession code is 1I84.

corrections

Genetic control and evolution of sexually dimorphic characters

Artyom Kopp, Ian Duncan, Dorothea Godt & Sean B. Carroll

Nature **408,** 553–559 (2000).

The name of one author, Dorothea Godt, was omitted from the author list but is included above. She is affiliated with the Department of Zoology, University of Toronto, Canada. In addition, a gene name was misspelled: the correct spelling is bric à brac. □

Mitochondrial genome variation and the origin of modern humans

Max Ingman, Henrik Kaessmann, Svante Pääbo & Ulf Gyllensten

Nature **408,** 708–712 (2000).

The complete mtDNA sequences upon which the analyses are based can be found at our website (http:/www.genpat.uu.se/mtDB/), dedicated to the analysis of complete mtDNA genomes of humans. The 53 sequences are also available in Genbank with the accession numbers AF346963–AF347015. □